Available online at www.sciencedirect.com
SCIENCE DIRECT®
Journal of Computational Physics 204 (2005) 430–461
JOURNAL OF COMPUTATIONAL PHYSICS
www.elsevier.com/locate/jcp

Modelling microstructural evolution of porous polycrystalline materials and a numerical study of anisotropic sintering

H.N. Ch'ng, J. Pan *

School of Engineering (H5), University of Surrey, Guildford, GU2 7XH, UK

Received 23 June 2004; received in revised form 12 October 2004; accepted 12 October 2004
Available online 21 November 2004

Abstract

This paper presents a numerical scheme for computer simulation of microstructural evolution of porous polycrystalline materials at elevated temperatures. The scheme is then applied to study the sintering behaviour of polycrystalline solid containing elongate pores. In a previous paper [J. Comput. Phys. 196 (2004) 724], we presented a set of finite element formulations to model surface diffusion, grain-boundary diffusion and grain-boundary migration, and their interactions. A range of numerical examples were provided for which analytical solutions are available to verify the finite element formulations. All these examples had to be simple and contained at most two grains for the analytical solutions to be possible. In this paper, we complete the numerical scheme and address the numerical issues which have to be resolved when applying the finite element formulations to material models consisted of many grains and pores. In particular, we demonstrate how the joining conditions at triple junctions are achieved in the finite element solution and how the microstructure is updated according to the velocities obtained from the finite element solution. The numerical scheme is then used to study the problem of anisotropic sintering. A series of computer simulations were carried out to study microstructural evolution around an elongate pore. The numerical results show that an elongate pore leads to anisotropic shrinkage and that the shrinkage is always larger in the direction of the longer axis of the pore. The numerical results also show that the shrinkage anisotropy can be controlled by manipulating the ratios between the kinetic mobilities of surface diffusion, grain-boundary diffusion and grain-boundary migration. Increasing the grain-boundary migration mobility increases the shrinkage anisotropy. Increasing the surface diffusion mobility, on the other hand, reduces the shrinkage anisotropy. These numerical findings are not obvious and remain to be verified by future experiment.

Keywords: Modelling; Computer simulation; Finite element analysis; Sintering; Solid-state diffusion; Anisotropy; Grain-boundary; Pore; Microstructural evolution

* Corresponding author. Tel.: +44 1483 68 6588/9671; fax: +44 1483 30 6039.
E-mail addresses: h.chng@surrey.ac.uk (H.N. Ch'ng), j.pan@surrey.ac.uk (J. Pan).

0021-9991/$ - see front matter © 2004 Elsevier Inc. All rights reserved.
doi:10.1016/j.jcp.2004.10.015

1. Introduction

At elevated temperatures, the microstructure of a polycrystalline solid evolves to reduce its total free-energy. Externally applied mechanical force can be a further driving force for such microstructural evolution. The kinetic mechanisms for the microstructural evolution depend on the material system, grain-size, temperature and level of the external stresses. Under many practical conditions, solid-state diffusion is a rate controlling mechanism for matter redistribution. Examples of microstructural evolution controlled by solid-state diffusion include Coble and Nabarro-Herring creep of engineering materials, cavity and crack growth in engineering materials and in interconnect lines of integrated circuits, sintering of fine particles and powder compacts, superplastic deformation of steels and alloys, diffusion bonding of similar or dissimilar materials and etc. In some of these examples, grain-growth also occurs simultaneously which is driven by the reduction of total grain-boundary energy. A common feature of all these examples is that the grain-boundaries as well as the free surfaces act as source and sink of matter in the microstructural evolution.

In recent years several different approaches have been developed to model microstructural evolution of materials. Using the classical finite difference method to solve the kinetic equations is the most natural approach which has been used widely [2–8]. The Monte-Carlo models (for example [9]) and the phase field models (for example [10–12]) are another two different approaches. Each of these approaches has its own advantages and disadvantages. It is inappropriate to review them here, but they all have difficulties to handle microstructurial evolution if the grain-boundaries act as source and sink of matter. In such a microstructural evolution, the grains move rigidly relative to each other as matter being either taken away or deposited onto a grain-boundary. Consequently, the microscopic velocity field of the material is discontinuous across any grain-boundary. Furthermore, the grain-boundary stresses, interfacial tensions and external loads have to satisfy the local and global equilibrium conditions. The velocity discontinuity and the global equilibrium conditions are difficult to handle using the finite difference method, the phase field model or the Monte-Carlo model. Microstructural evolution with a discontinuous velocity field is best handled using a fourth approach – the discrete element method based on a variational principle. Needleman and Rice [13] developed a variational principle for grain-boundary diffusion and power law creep. Cocks [14] was the first to develop a discrete finite element scheme using the variational principle for grain-boundary diffusion problem in hexagonal grain structures. Later Pan, Cocks and their co-workers [15–17] developed finite element formulations for grain-boundary diffusion, surface diffusion and grain-boundary migration. Sun and Suo [18,19], Bänsch et al. [20], have also developed weak solutions and finite element schemes for similar problems. However, these finite element formulations used linear shape functions for the migrating velocity of the interface which is numerically inefficient and has limited their applications to problems of a few interfaces. Recently, Chen et al [21] developed a grid based numerical scheme using the variational approach but their method is limited to grain-growth.

In a previous paper [1], we presented a set of finite element formulations using the classical cubic spline as the shape functions to model surface diffusion, grain-boundary diffusion and grain-boundary migration. A range of numerical examples were provided for which analytical solutions are available to verify the formulations. The cubic spline elements make it possible to model an interface using as few as three elements hence opened the door to modelling microstructural evolution using realistic material models consisted of thousands of grains. Due to space limit in the previous paper, we could not address the numerical issues which have to be resolved when applying the finite element formulations to material models consisted of many grains and pores. Neither was it possible to present applications of the numerical scheme to such problems. This is where the current paper begins. In the current paper, we demonstrate how the joining conditions at triple junctions are achieved in the finite element solution and how the microstructure is updated according to the velocities obtained from the finite element solution. The numerical scheme is then used to study the problem of anisotropic sintering. A series of computer simulations were carried out to study microstructural evolution around an elongate pore. The numerical results show that the elongate

pore leads to anisotropic shrinkage and that the shrinkage is always larger in the direction of the longer axis of the pore. The numerical results also show that the shrinkage anisotropy can be controlled by manipulating the ratios between the kinetic mobilities of surface diffusion, grain-boundary diffusion and grain-boundary migration. Increasing the grain-boundary migration mobility increases the shrinkage anisotropy. Increasing the surface diffusion mobility, on the other hand, reduces the shrinkage anisotropy. These numerical findings are not obvious and remain to be verified by future experiment.

2. A brief summary of the variational model and the finite element scheme

Fig. 1 shows schematically the problem addressed in this paper. A two-dimensional representative unit of a polycrystalline material containing pores is considered. At elevated temperatures the microstructure evolves to reduce its total potential energy E, which is defined as

$$E = \int_{\Gamma_{gb}} \gamma_{gb}\, d\Gamma + \int_{\Gamma_s} \gamma_s\, d\Gamma - \int_{\Gamma_F} \boldsymbol{F}\cdot\boldsymbol{U}\, d\Gamma, \tag{1}$$

in which γ_{gb} and γ_s represent the specific energies for the grain-boundaries and free surfaces, respectively (which can be orientation and location dependant), Γ_{gb} represents the grain-boundary network, Γ_s the free surfaces, Γ_F the boundary of the representative unit where a distributed force $\boldsymbol{F}$ is applied, and $\boldsymbol{U}$ the displacement of Γ_F with respect to a reference configuration. The grain-boundaries can migrate leading to grain-growth and reducing the total grain-boundary energy. The network of grain-boundaries and free surfaces act as a short-cut for solid-state diffusion as well as source or sink of matter. Matter redistribution between the grain-boundaries and the free surfaces makes the free surfaces migrate and the pores grow or shrink. Simultaneously, matter redistribution within the grain-boundaries makes the grains move relatively to each other and causes extra migration of the grain-boundaries in addition to the grain-growth

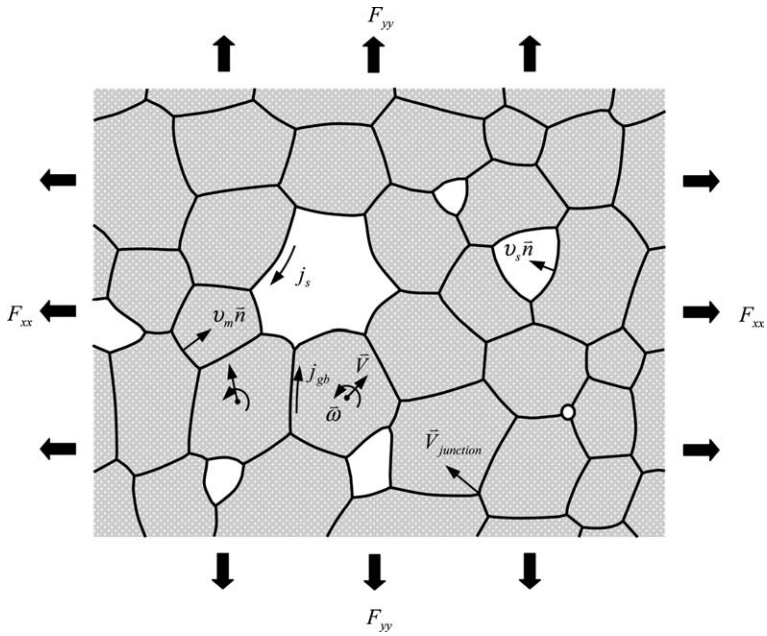

Fig. 1. A representative unit of a polycrystalline material containing pores.

mentioned above. If the applied load is small or does not exist, it has been generally accepted that the elastic stresses quickly diminish as material is being redistributed and the elastic deformation of the grains can be ignored. In our model the grains are assumed to be rigid. The macroscopic deformation of the material comes completely from the collection of the rigid motions of the grains, which is often referred to as Coble creep when pores are not involved.

The diffusive flux, defined as volume of matter flowing along the interface across unit slab thickness of the interface per unit time, is referred to as j_{gb} for grain-boundary diffusion and j_s for surface diffusion. The migrating velocity is referred to as v_m for a grain-boundary and v_s for a free surface. The matter redistribution and the evolution of the interfaces are governed by a variational principle, that is, among all the possible diffusive fluxes and migration velocities which satisfy matter conservation, the true fluxes and velocities make a functional Π^* stationary,

$$\Pi^* = \int_{\Gamma_{gb}} \frac{1}{2M_{gb}} j_{gb}^2 \, d\Gamma + \int_{\Gamma_s} \frac{1}{2M_s} j_s^2 \, d\Gamma + \int_{\Gamma_{gb}} \frac{1}{2M_m} v_m^2 \, d\Gamma + \frac{dE}{dt} + \sum \lambda_j \left(\sum j \right) + \sum \lambda_{v'} \left(\sum v'' \right) + \sum \lambda_{v''} \left(\sum v'' \right), \tag{2}$$

in which M_{gb}, M_s and M_m represent the mobilities of grain-boundary diffusion, surface diffusion and grain-boundary migration, respectively. Needleman and Rice [13] developed the original version of this variational principle. Cocks [14], Suo and Wang [22], Sun et al. [18], Cocks and Gill [23] and Pan et al. [16] extended it to include surface diffusion, lattice diffusion and grain-boundary migration. Ch'ng and Pan [1] included the last two Lagrange terms to enforce the continuity of the first and second derivatives of the migrating velocity across all the finite element nodes except for the triple junctions.

In a previous paper [1], we developed a set of parametric finite element formulations for surface diffusion, grain-boundary diffusion and grain-boundary migration. The classical cubic spline was used to approximate the interfaces as well as the shape functions for the migrating velocities of the interfaces. Special elements were developed to deal with the triple junctions. Using the classical finite element approach, functional Π was discretised as

$$\Pi^* = \frac{1}{2}[U]^T[A][U] + [F][U], \tag{3}$$

in which $[U]$ is a vector of global unknowns containing (as shown in Fig. 1):

- $\vec{V}$ and $\vec{\omega}$ – the velocities of rigid motion of the grains,
- $V_{junction}$ – velocities of all the triple junctions,
- v_s and v_m – nodal migration velocities of free surfaces and grain-boundaries,
- c_v and d_v – parameters for cubic spline representation of the migrating, velocity, defined for each element,
- j_s and j_{gb} – diffusive fluxes across at all the mid-points of surface and grain-boundary diffusion elements,
- λ_j, $\lambda_{v'}$, $\lambda_{v''}$ – Lagrange multipliers. The first one is defined at all the finite element nodes and triple junctions to enforce flux conservation, the last two are defined at all the finite element nodes except for triple junctions to enforce continuity of the first and second derivatives of the migrating velocity.

$[A]$ is a generalised global viscosity matrix and $[F]$ is the global force vector.
$\delta\Pi* = 0$ leads to

$$[A][U] + [F] = 0, \tag{4}$$

from which $[U]$ can be solved using a standard numerical solver. The finite element formulations were verified using six different testing cases for which analytical solutions are available.

3. Joining conditions at triple junctions

At a triple junction where three interfaces meet each other, there are three joining conditions:

(a) the diffusive fluxes must be conserved,
(b) the chemical potential must be continuous, and
(c) interfacial tensions must be balanced with each other.

In the variational model, the continuity of diffusive fluxes at any triple junction is satisfied by the first Lagrange multiplier term (λ_j) in the functional Π^* given by Eq. (2). Furthermore, the Lagrange multiplier λ_j turns out to be the chemical potential and the fact that the three joining interfaces at a triple junction share a common Lagrange multiplier satisfies the continuity of the chemical potential. The equilibrium between the interfacial tensions make the interfaces meet at fixed angles. For example, the equilibrium between the grain-boundary tension and the free surface tensions as shown in Fig. 2 leads to an equilibrium dihedral angle ψ which is given by

$$\cos\left(\frac{\psi}{2}\right) = \frac{\gamma_{\mathrm{gb}}}{2\gamma_{\mathrm{s}}} \tag{5}$$

in which γ_{s} and γ_{gb} are specific energies for the free surface and grain-boundary, respectively. Fig. 3 shows a slightly complicated example. Two infinitively long grains sit on a single crystal substrate. The interface between the right grain and the substrate is assigned a higher specific energy than that between the left grain and the substrate, i.e., $\gamma_{\mathrm{sb}_1} > \gamma_{\mathrm{sb}_2}$. The vertical grain-boundary migrates to the right to reduce the total free energy of the system. At the steady state, the grain-boundary move to the right with a constant velocity and the profile of the grain-boundary and triple junction remains unchanged as illustrated in Fig. 3. Mullins [24,25] showed that the profile of the top triple junction is independent of the migrating velocity and provided the steady state angle of ψ_B as

$$\psi_B = \frac{\gamma_{\mathrm{gb}}}{6\gamma_{\mathrm{s}}}. \tag{6}$$

Suo [26] obtained that

$$\psi_C = \frac{\pi}{2} - \frac{\gamma_{\mathrm{sb}_1} - \gamma_{\mathrm{sb}_2}}{\gamma_{\mathrm{gb}}}, \tag{7}$$

while ψ_A is determined from Eq. (5). For numerical schemes which are not based on the variational approach, the equilibrium condition between the interfacial tensions has to be enforced as part of the boundary conditions. For a recent example, see the work by Zhang et al. [8] in which they carefully implemented all the joining conditions and criticised the joining conditions used by Pan and Cocks in their earlier work [27]. The criticisms were valid that Pan and Cocks did not allow the triple junction to rotate. However, the criticism that there was no continuity of chemical potential at the triple junction in the Pan–Cocks model

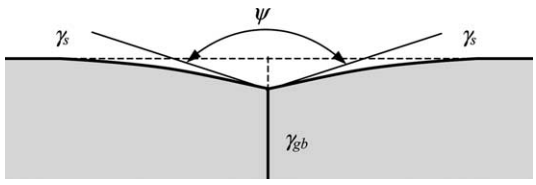

Fig. 2. A triple junction where a grain-boundary meets a free surface.

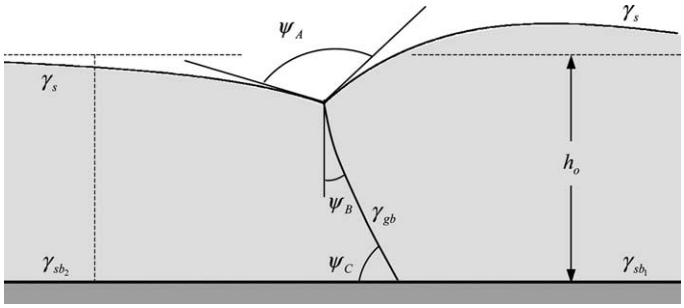

Fig. 3. Thermal grooving by surface diffusion at a migrating grain-boundary with the symbolic definitions for specific energies and the three angles of our interest, ψ_A, ψ_B and ψ_C.

was a misunderstanding of their work. Pan and Cocks used a so-called tip curvature which was shared between the grain-boundary and the free surface at the junction and therefore guaranteed the continuity of the chemical potential.

For the variational model, Suo [26] pointed out that the equilibrium condition between interfacial tensions is a natural boundary condition which comes out of the variational principle and does not need to be enforced exactly. This is an analogy to the force boundary conditions in an elasticity problem which is satisfied indirectly by the minimisation of the total potential energy of the system. Suo [26], however, did not prove the variational argument for the general case where three interfaces meet at arbitrary angles. Considering three interfaces joining at a junction as shown in Fig. 4 the motion of the triple junction and adjustment of the angles at which the three interfaces meet can be realised by grain-boundary migration and/or surface diffusion. Surface diffusion can be further coupled to grain-boundary diffusion, but for simplicity we ignore grain-boundary diffusion in the following derivation. We also drop all the Lagrange terms in Eq. (2) since they are irrelevant here. Carrying out a variational calculation to Π^* we have

$$\delta\Pi^* = \int_{\text{free-surface}} \frac{j_s}{M_s}\delta j_s \, d\Gamma + \int_{\text{grain-boundary}} \frac{v_m}{M_m}\delta v_m \, d\Gamma + \delta\left(\frac{dE}{dt}\right). \tag{8}$$

Here, $\delta\dot{E}$ represents the virtual change of the free energy rate which can be calculated as

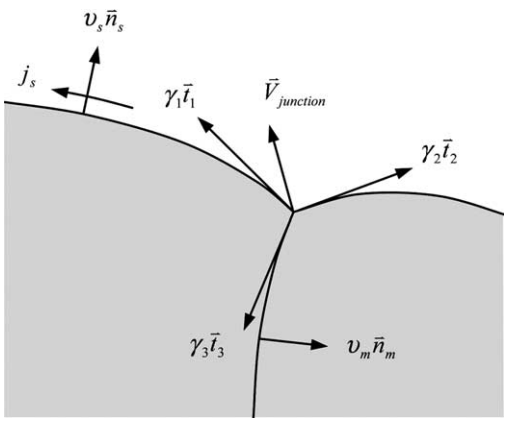

Fig. 4. Equilibrium of interfacial tensions at a triple junction.

$$\delta\left(\frac{\mathrm{d}E}{\mathrm{d}t}\right) = \delta\left(-\int_{\text{free-surface}} \gamma_s\kappa_s v_s \,\mathrm{d}\Gamma - \int_{\text{grain-boundary}} \gamma_{gb}\kappa_{gb} v_m \,\mathrm{d}\Gamma - \left(\gamma_1 \vec{t}_1 + \gamma_2 \vec{t}_2 + \gamma_3 \vec{t}_3\right)\cdot \vec{V}_{\text{junction}}\right)$$
$$= -\int_{\text{free-surface}} \gamma_s\kappa_s \delta v_s \,\mathrm{d}\Gamma - \int_{\text{grain-boundary}} \gamma_{gb}\kappa_{gb}\delta v_m \,\mathrm{d}\Gamma - \left(\gamma_1 \vec{t}_1 + \gamma_2 \vec{t}_2 + \gamma_3 \vec{t}_3\right)\cdot \delta\vec{V}_{\text{junction}}, \quad (9)$$

in which κ_s and κ_{gb} are the principal curvatures of the free surface and the grain-boundary, respectively. The sign conventions for the principal curvature and migrating velocities are such that a reduction in the interfacial area leads to a negative $\dot{E}$. Matter conservation requires that

$$v_s + \frac{\partial j_s}{\partial \Gamma} = 0, \quad (10)$$

from which we have

$$\int_{\text{free-surface}} \gamma_s\kappa_s\delta v_s \,\mathrm{d}\Gamma = \int_{\text{free-surface}} \gamma_s\kappa_s\left(-\frac{\partial(\delta j_s)}{\partial\Gamma}\right)\mathrm{d}\Gamma = \int_{\text{free-surface}} \frac{\partial(\gamma_s\kappa_s)}{\partial\Gamma}\delta j_s \,\mathrm{d}\Gamma. \quad (11)$$

Combining Eqs. (8), (9) and (11), we obtain

$$\delta\Pi^* = \int_{\text{free-surface}} \left(\frac{j_s}{M_s} - \frac{\partial(\gamma_s\kappa_s)}{\partial\Gamma}\right)\delta j_s \,\mathrm{d}\Gamma + \int_{\text{grain-boundary}} \left(\frac{v_m}{M_m} - \gamma_{gb}\kappa_{gb}\right)\delta v_m \,\mathrm{d}\Gamma$$
$$- \left(\gamma_1 \vec{t}_1 + \gamma_2 \vec{t}_2 + \gamma_3 \vec{t}_3\right)\cdot \delta\vec{V}_{\text{junction}}. \quad (12)$$

Because δj_s, δv_m and $\delta\vec{V}_{\text{junction}}$ are arbitrary variations, for $\delta\Pi^* = 0$ we must have

$$j_s = M_s\frac{\partial(\gamma_s\kappa_s)}{\partial\Gamma}, \quad (13)$$

$$v_m = M_m\gamma_{gb}\kappa_{gb}, \quad (14)$$

and

$$\gamma_1 \vec{t}_1 + \gamma_2 \vec{t}_2 + \gamma_3 \vec{t}_3 = 0. \quad (15)$$

Eqs. (13) and (14) are the kinetic equations for surface diffusion and grain-boundary migration. Eq. (15) is the equilibrium condition of the interfacial tensions at the junction. Therefore, the equilibrium of the interfacial tensions, as well as the kinetic equations, comes out of the variation which means that the numerical solution to the linear simultaneous Eq. (4) is such that the equilibrium conditions at all the triple junctions are satisfied to the best ability of the available degrees of freedom in the finite element model. This is demonstrated in the following numerical examples.

Figs. 5 and 6 show our numerical solutions for the thermal grooving process by surface diffusion as defined in Fig. 2 using two different finite element meshes. The numerical analysis started from an initially flat top surface. A ratio of $\gamma_s/\gamma_{gb} = 1$ was used in the example and the time is normalised as $\bar{t} = \frac{M_s\gamma_s}{h^4}t$. Mullin's steady state solution [25] is also presented in the figures using discrete dots for comparison. Fig. 7 shows the evolution of the dihedral angle with respect to the normalised time obtained using the coarse and fine-mesh, respectively. It can be seen that the finite element solution does indeed recover and then maintain the correct dihedral angle of 120° as given by Eq. (5). However, the time required by the recovery is sensitive to the mesh size. The fine-mesh model recovered the dihedral angle over three orders of magnitude faster than the coarse-mesh one did. It is then interesting to observe that the overall evolution of the interfaces is not significantly affected by this sensitivity. Figs. 5 and 6 show that both the coarse-mesh solution and the fine-mesh solution agree very well with the Mullins solutions. This is because the dihedral angle is an issue very local to the triple

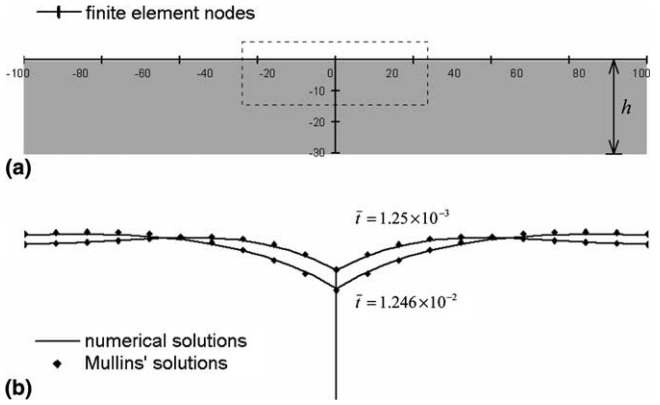

Fig. 5. Comparison between a coarse-mesh finite element solution (solid lines) and the steady state solution by Mullins (discrete dots) for thermal grooving problem by surface diffusion. (a) Finite element mesh and the initial profile and (b) grooved profiles of the zoomed-in region as shown in (a) using the dashed box at two different times of $\bar{t} = 1.25 \times 10^{-3}$ and $\bar{t} = 1.246 \times 10^{-2}$.

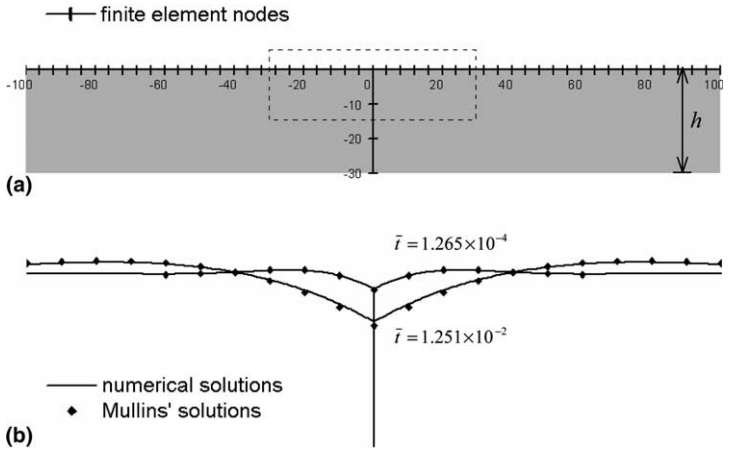

Fig. 6. Comparison between a fine-mesh finite element solution (solid lines) and the steady state solution by Mullins (discrete dots) for thermal grooving problem by surface diffusion. (a) Finite element mesh and the initial profile and (b) grooved profiles of the zoomed-in region as shown in (a) using the dashed box at two different times of $\bar{t} = 1.265 \times 10^{-4}$ and $\bar{t} = 1.251 \times 10^{-2}$.

junction. This numerical finding is important because it means that one does not have to use extremely fine-meshes to look after the dihedral angle. Fig. 8 presents our numerical solutions of the three angles ψ_A, ψ_B and ψ_C as defined in Fig. 3 as functions of time. The finite element simulation started from a vertical grain-boundary and a flat top surface (the dotted lines in Fig. 3). Following parameters were used in the example: $\gamma_{gb}/\gamma_s = 1$, $\gamma_{sb_1}/\gamma_s = 1.5$, $\gamma_{sb_2}/\gamma_s = 1$ and $M_m h_0^2/M_s = 10.4$. Using these data, Eqs. (5)–(7) predict that $\psi_A = 120°$, $\psi_B = 9.55°$ and $\psi_C = 61.35°$ which can be compared with the values approached by the finite element solutions of $\psi_A = 120°$, $\psi_B = 11°$ and $\psi_C = 63°$. Fig. 9 shows the evolutions of the two triple junctions (*a*, *b* and *c*, for the top triple junction and *d*, *e* and *f* for the bottom one). These numerical examples show that the variational principle does indeed lead to the correct angles at which the interfaces meet and therefore the equilibrium of interfacial tensions at the triple junctions.

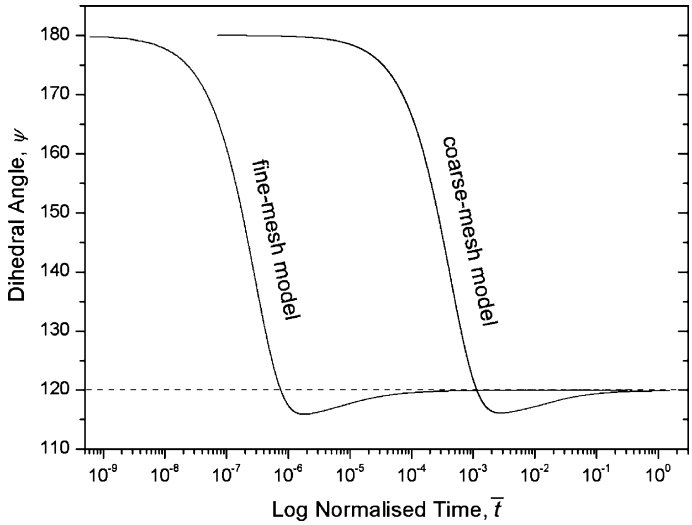

Fig. 7. The dihedral angle as function of time obtained using the fine and coarse finite element meshes, respectively, for the thermal grooving problem shown in Fig. 2.

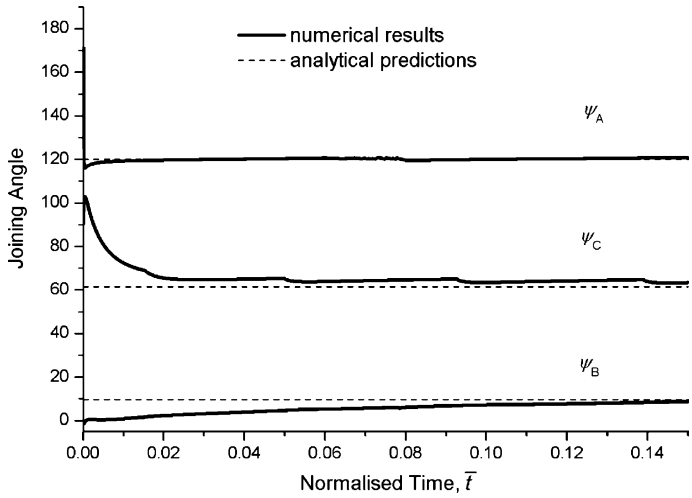

Fig. 8. The angles of ψ_A, ψ_B and ψ_C as defined in Fig. 3 as functions of time obtained from the finite element analysis. Also in the figure, the predictions of Eqs. (5)–(7) are shown as dashed lines.

4. Updating the microstructure

For simplicity the direct Euler scheme is adopted here for time integration. The finite element analysis starts from an initial network of grain-boundaries and free surfaces. Each interface is approximated using a cubic spline containing a set of finite elements. At each time step, the linear simultaneous equation (4) is constructed and solved providing all the degree of freedoms in $[U]$ as listed in Section 2. Then the entire network of the interfaces including the positions of the triple junctions is updated according to $[U]$. Finally, a new cubic spline is constructed for each interface from the updated profile. This procedure is repeated

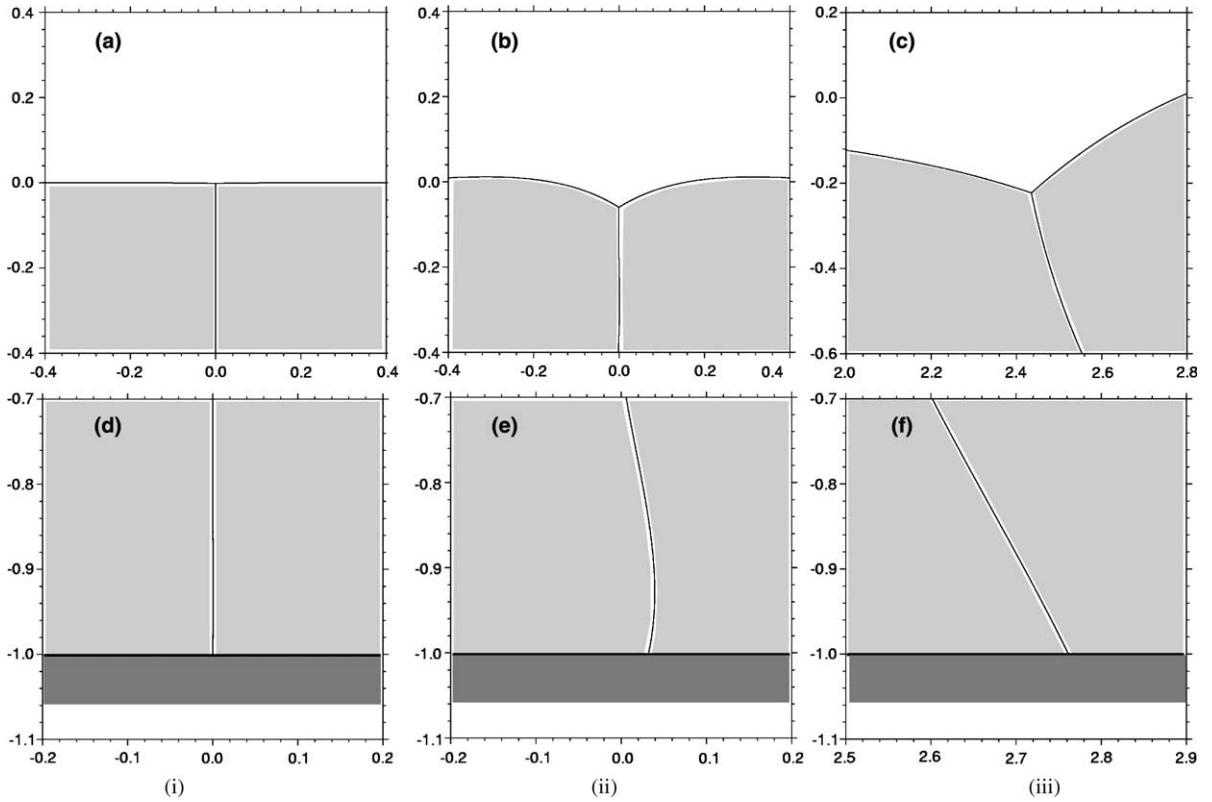

Fig. 9. Numerically obtained evolutions of the two triple junctions for the problem defined in Fig. 3. (i) $\bar{t} = 1.166 \times 10^{-6}$, (ii) $\bar{t} = 3.031 \times 10^{-4}$ and (iii) $\bar{t} = 4.0 \times 10^{-1}$.

until a required time or characteristic of the microstructural evolution is reached. The rigid motion of the grains makes the updating procedure less straightforward especially at the triple junctions. These updating steps are discussed in detail in the following sections.

4.1. Updating the interface profile and triple junction positions

The profile of an interface is represented by a collection of location vectors $\vec{r}_i,\ i = 1, 2, \ldots, m$, at a series of points on the interface as shown in Fig. 10. Because the cubic spline formulations allow one to use very coarse finite element mesh, m has to be much larger than the total number of finite element nodes on any interface to represent the interface accurately. Some of these points coincide with the finite element nodes and the triple junctions. At each time step a location vector is updated according to its velocity $\vec{V}_i$:

$$\vec{r}_i(t + \Delta t) = \vec{r}_i(t) + \vec{V}_i \times \Delta t \tag{16}$$

in which Δt is a small time step. The velocity $\vec{V}_i$ consists of two parts – the migrating velocity of this point and the rigid motion of the grain or grains associated with the point. The migrating velocity is always along the direction of the normal vector, $\vec{n}_i$, to the interface as shown in Fig. 1. Solving Eq. (4) provides all the nodal values of the migrating velocities (υ_m and υ_s) and the cubic spline parameters (c_υ and d_υ) from which the values of υ_m and υ_s can be determined at any point of the interface [1]. The velocity of point i due to the rigid motion of its associated grain, $\vec{V}_{\text{rigid},i}$, can be calculated as

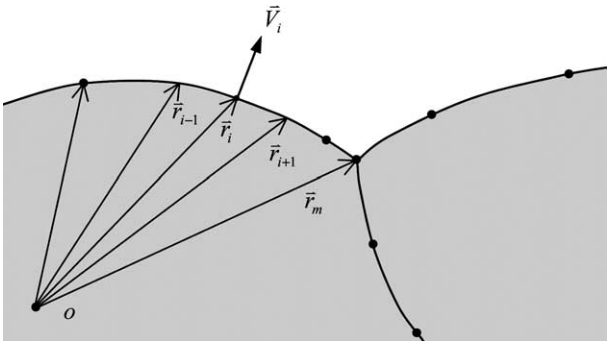

Fig. 10. A collection of location vectors $\vec{r}_i$ to represent an interface.

$$\vec{V}_{\text{rigid},i} = \vec{V}_{\text{centre}} + \vec{\omega} \times \vec{r}_{oi}, \tag{17}$$

in which $\vec{V}_{\text{centre}}$ and $\vec{\omega}$ are the translational and rotational velocities of the grain, and $\vec{r}_{oi}$ is a vector linking the centre O of the grain to node i under concern. V_{centre} and $\vec{\omega}$ are obtained by solving Eq. (4). For a point on a free surface, its total velocity is then given by

$$\vec{V}_i = \upsilon_s \vec{n}_i + \vec{V}_{\text{rigid},i}. \tag{18}$$

Each point on a grain-boundary is associated with two grains on either side of the grain-boundary as shown in Fig. 11. As matter is being redistributed along the grain-boundary, the two grains move relatively to each other causing the grain-boundary to reposition itself. This extra migrating velocity of the point is taken as the average of the two velocities of this point due to the rigid motion of the two grains, respectively, i.e. we have

$$\vec{V}_i = \upsilon_m \vec{n}_i + \left(\vec{V}^1_{\text{rigid,i}} + \vec{V}^2_{\text{rigid},i} \right) \Big/ 2. \tag{19}$$

The extra migrating velocity of a triple junction due to the rigid motions of grains surrounding the junction can be calculated in similar way and the total velocity of the triple junction can be calculated as

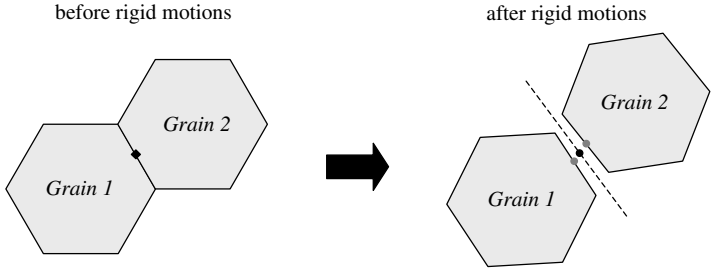

- initial position of point *i* between *Grain 1* and *Grain 2*
- new position of point *i* averaged from the rigid motion of *Grain 1* and *Grain 2*
- positions of point *i* due to the rigid motions from *Grain 1* and *Grain 2* respectively

Fig. 11. Migration of a grain-boundary due to grain-boundary diffusion.

$$\vec{V}_i = \vec{V}_{\text{triple},i} + \begin{cases} \left(\vec{V}^{1}_{\text{rigid},i} + \vec{V}^{2}_{\text{rigid},i}\right)\Big/2 & \text{surface\_gb\_junction}, \\ \left(\vec{V}^{1}_{\text{rigid},i} + \vec{V}^{2}_{\text{rigid},i} + \vec{V}^{3}_{\text{rigid},i}\right)\Big/3 & \text{triple\_gb\_junction}. \end{cases} \tag{20}$$

in which $\vec{V}_{\text{triple},i}$ is the velocity of the triple junction which is obtained by solving Eq. (4). We have, however, used a different approximation of the extra velocity taking into account of not only the rigid motions of the triple junction but also the tangent of the extra grain-boundary migration in the vicinity of the junction. This is illustrated in Figs. 12 and 13 using a simple example of straight grain-boundaries. At each time step, the profiles of the three joining grain-boundaries are updated using Eq. (19) but without the term of $\upsilon_{\text{m}}\vec{n}_i$. This is indicated by *GB1*, *GB2*, and *GB3* in Fig. 12. The updated three grain-boundaries do not usually meet at a common point. Each grain-boundary is then extended along its tangent direction as shown in Fig. 13. The three intersecting points between the three extended grain-boundaries are determined and the new triple junction is located at the average location of the three intersecting points. Finally, the location of the triple junction is updated again using its migrating velocity $\vec{V}_{\text{triple},i}$. A triple junction between a free surface and a grain-boundary is updated in the similar way.

4.2. Reconstructing cubic spline elements and remeshing

In the finite element formulations, a set of cubic spline elements are used to represent each interface. Fig. 14 shows such an element for which we have

$$x_j(\zeta) = \begin{bmatrix} N_1(\zeta) & N_2(\zeta) & N_3(\zeta) & N_4(\zeta) \end{bmatrix} \begin{bmatrix} x_{1,j} \\ x_{2,j} \\ c_{xj} \\ d_{xj} \end{bmatrix}, \tag{21}$$

and

$$y_j(\zeta) = \begin{bmatrix} N_1(\zeta) & N_2(\zeta) & N_3(\zeta) & N_4(\zeta) \end{bmatrix} \begin{bmatrix} y_{1,j} \\ y_{2,j} \\ c_{yj} \\ d_{yj} \end{bmatrix}, \tag{22}$$

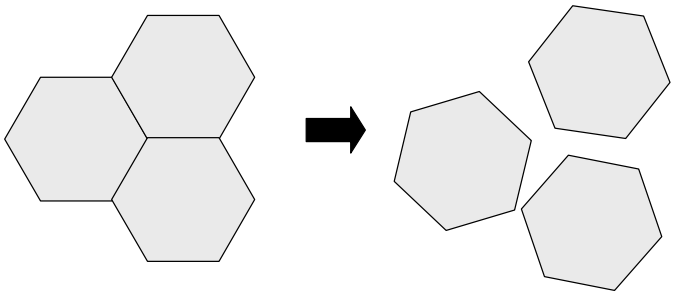

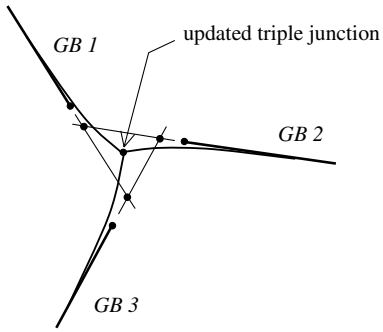

Fig. 13. Reposition of a triple junction as a consequence of the rigid motion of the grains surrounding the junction.

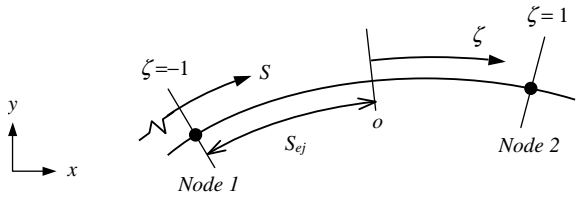

Fig. 14. Symbolic definitions of a cubic spline element.

in which $x_{1,j}$, $x_{2,j}$, $y_{1,j}$ and $y_{2,j}$ are the coordinates of the two nodes; c_{xj}, c_{yj}, d_{xj} and d_{yj} are the cubic spline parameters; and $N_1(\zeta)$, $N_2(\zeta)$, $N_3(\zeta)$ and $N_4(\zeta)$ are the shape functions given by

$$\begin{aligned} N_1(\zeta) &= \frac{1}{2}(1-\zeta), \\ N_2(\zeta) &= \frac{1}{2}(1+\zeta), \\ N_3(\zeta) &= S_{ej}^2(\zeta^2-1), \\ N_4(\zeta) &= S_{ej}^3[(1+\zeta)^3 - 4(1+\zeta)], \end{aligned} \tag{23}$$

in which ζ is a local coordinate defined in Fig. 14 and S_{ej} is the half length of element j.

At each time step, the profile of all the interfaces is updated as discussed in Section 4.1. An updated interface is no longer necessarily a cubic spline. For the finite element analysis to continue, a new cubic spline has to be constructed for each interface (i.e. to determine c_{xj}, c_{yj}, d_{xj} and d_{yj} for all the elements on an interface). The classical procedure to construct a cubic spline in the form of Eqs. (21)–(23) requires the coordinates of the finite element nodes, the lengths of all the elements $2S_{ej}$, and the boundary conditions of $dx/d\zeta$ and $dy/d\zeta$ at the two ends of the interface. The coordinates of all the finite element nodes including the triple junctions are obtained as part of the location vectors $[\vec{r}_i]$ as discussed in Section 4.1. The half elemental length S_{ej} is calculated from $[\vec{r}_i]$ by numerical integration. Finally, the boundary values of $dx/d\zeta$ and $dy/d\zeta$ are calculated from $[\vec{r}_i]$ at the two ends of the interface by numerical differentiation. We have used typically between 30 and 50 integration points within each element to calculate S_{ej}. Our experience shows that the accuracy of the boundary values of $dx/d\zeta$ and $dy/d\zeta$ has a critical influence on the fast recovery of the dihedral angles at triple junctions. It is necessary to numerically calculate $dx/d\zeta$ and $dy/d\zeta$ at a number of points on an interface near a triple junction and then linearly extrapolate the numerical results to the triple junction to obtained the correct boundary values of $dx/d\zeta$ and $dy/d\zeta$. It seems tedious to have to reconstruct the cubic splines at each time step. However, the procedure is automatic and repeating the procedure does not

pose much extra programming effort after one has done it once. Nevertheless using the cubic spline elements increases the complexity of the numerical procedure in comparison with the simple linear elements. However, in a numerical simulation using the linear elements for surface diffusion in particular, most of the computing time is spent on the oscillation of the nodal positions, while the cubic spline scheme moves the surface forward with much less oscillation. Our numerical experience showed that the extra complexity of the cubic spline elements far out balances the numerical instability of the linear elements. It is usual for the cubic spline elements to achieve a stable numerical solution several order of magnitudes faster than the linear elements in terms of the computing time.

As most of the problems that we are interested in involves large scale microstructural evolution, frequent remeshing of the interfaces has to be carried out automatically for the computer simulation to continue. An element, interface or even entire grain can be deleted from the microstructure if any of them becomes too short or small. A new element has to be added where an element becomes too long. Fig. 15 shows an actual example of the remeshing process near a triple junction for a simulation of the co-sintering process of two particles. The criteria for remeshing (i.e. the definitions for two short or too long) are, however, empirical. The choice of the allowed minimum and maximum lengths of the elements or interfaces should be such that further decreasing them would not make any difference to the numerical results. From our numerical experience, we found that this can be achieved by setting the minimum and maximum elemental lengths at 25% and 160% of the average length of all the elements, respectively.

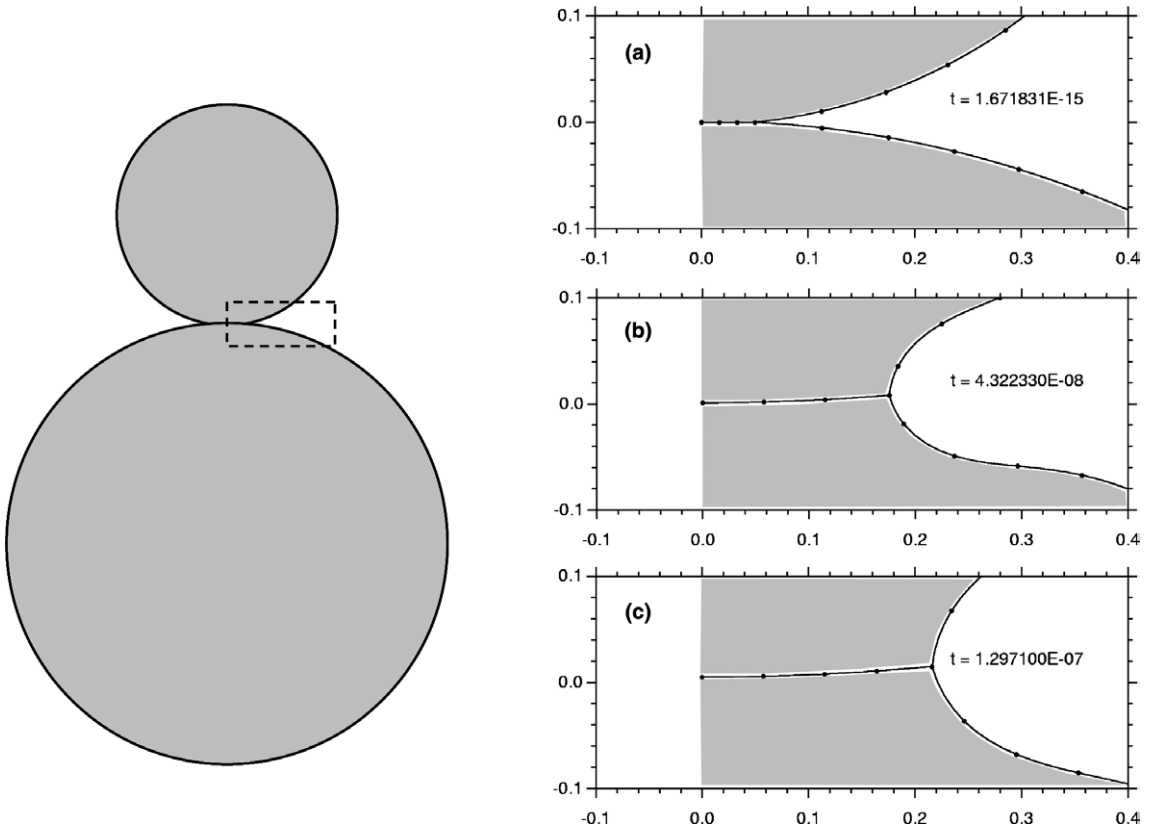

Fig. 15. Remeshing of three interfaces joining at a triple junction for the sintering problem. As sintering proceeds, some elements were added to the grain-boundary and deleted from the free surfaces.

In order to verify and demonstrate the updating procedures discussed above, we present a case of superplastic deformation of initially hexagonal grains as shown in Fig. 16. Grain-boundary diffusion is assumed as the only rate controlling mechanism in this example. Spingarn and Nix [4] provided an analytical solution for the problem and obtained the strain rate of the material when a remote stress σ is applied in the vertical direction as

$$\dot{\varepsilon} = \frac{144 M_{\mathrm{gb}}}{d_0^3} \frac{\exp \varepsilon}{[3 - \exp 2\varepsilon]^2} \sigma \tag{24}$$

in which M_{gb} is the grain-boundary diffusion mobility, d_0 is the initial grain size as defined in Fig. 16(a), and ε is the true strain in the vertical direction.

Figs. 16(b) and (c) show the computer simulated microstructural evolution of the superplastic deformation using our finite element scheme and updating procedure. In the numerical analysis, all the length scales are normalised by d_0, and the time is normalised as $\bar{t} = \frac{M_{\mathrm{gb}}\gamma_{\mathrm{gb}}}{d_0^4} t$. A normalised remote stress of $\bar{\sigma} = (\sigma d_0)/\gamma_{\mathrm{gb}} = 1.5 \times 10^6$ was applied in the vertical direction. Fig. 17 shows the comparison between the finite element results and the prediction of Eq. (24) for the true strain in the vertical direction as a function of the normalised time. Perfect agreement was obtained showing that the finite element formulation and the updating procedure are both working.

5. A numerical study of anisotropic sintering

In this section, we use the numerical scheme to study an important industrial problem – the anisotropic deformation of powder compacts during sintering. Sintering is a process in which a fragile powder compact is fired producing a strong solid. Most of the ceramic products and an increasing number of metal, polymer and glass components are made by sintering. Recently, Pan has provided a critical review of the existing

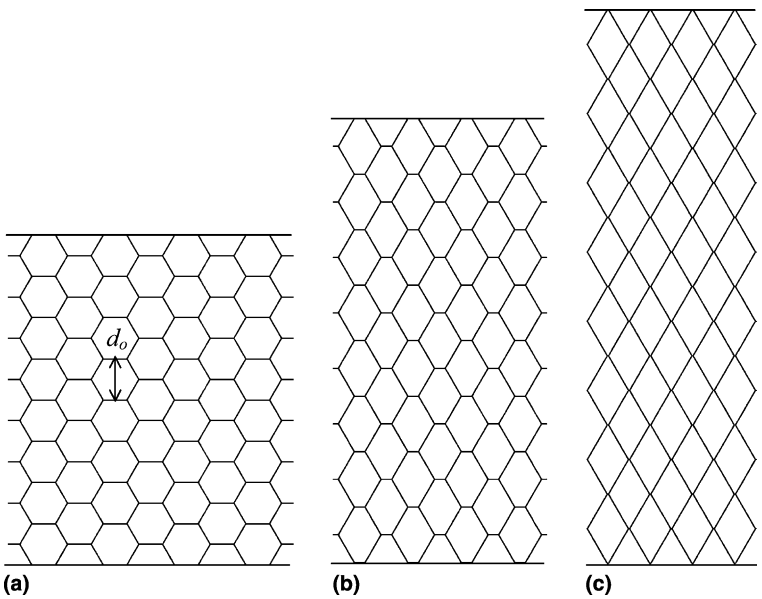

Fig. 16. Computer simulated superplastic deformation of an initially hexagonal microstructure. Grain-boundary diffusion is the only operating mechanism in this example. A remote vertical stress is applied. Each grain-boundary was modelled using three cubic spline elements. (a) $\bar{t} = 0$, (b) $\bar{t} = 3.3 \times 10^{-9}$, and (c) $\bar{t} = 3.752 \times 10^{-9}$.

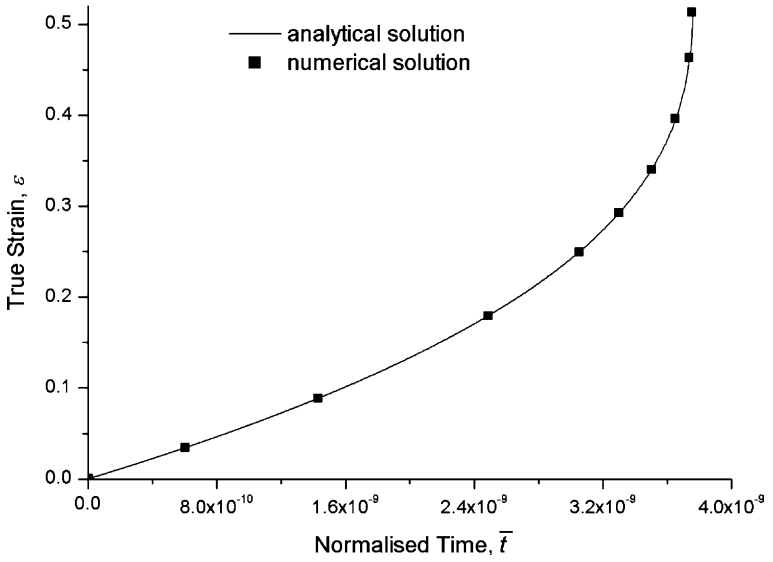

Fig. 17. Comparison between numerical and analytical solutions of the true strain as a function of time for the superplastic deformation of a hexagonal structure.

sintering models at atomic, microscopic and continuum levels [28]. Practical experiences have shown that shrinkage during sintering is usually anisotropic. Taking the simplest case of sintering a cylindrical sample as an example, it has been widely observed that the shrinkage in the axial direction differs from that in the radial direction [29]. Dimensional control is a fundamental issue in ceramic and powder metallurgy (PM) processing. The anisotropic shrinkage poses a serious problem to the commercial production of ceramic and PM products. There have been many experimental studies on the anisotropic shrinkage and two factors appear to be the major causes for the anisotropic behaviour. The first factor is that elongate particles arrange themselves in a preferred orientation in processes like tape casting, injection moulding or compaction prior to sintering which has been reported by Sanchez [30], Mitomo et al. [31], Huber et al. [32], Zhang et al. [33], Uematsu et al. [34], Greenwood et al. [35], Raj and Cannon [36], Raj et al. [37] and Shui et al. [38–40]. Recently, Raj et al. [37] proposed a numerical model for the sintering of elongate particles which predicts that compact consisted of aligned elongate particles shrink faster in the direction of the shorter axis of the particles and that the shrinkage anisotropy reduces as sintering progresses. These predictions are in general agreement with experimental observations [36]. However, many experimental data have shown that the shrinkage is anisotropic for non-elongate and even spherical powders. The cause for the anisotropic shrinkage in these powders is believed to be elongate pores. Roman and Hausner [41], Hausner [42], Exner [43], Mitkov et al. [44] and Rahaman and De Jonghe [45] have all concluded that oriented pores are the cause for the anisotropic shrinkage which they observed. The orientation of pores and the extent of pore elongation are sensitive to the compaction method [43,44], the level of the pressure [46] and even the size distribution of the particles [41]. Moon and Huppmann [47] on the other hand observed that the shrinkage anisotropy reduces as sintering enters the final stage. There have been very few modelling efforts to understand the fundamentals of the anisotropic shrinkage caused by elongate pores. Jagota et al. [48] considered a powder compact in which the number of contacts is orientation dependent and developed an anisotropic constitutive law which is suitable for early stage sintering. Olevsky and Skorohod [49] considered a viscous solid containing elliptical and periodically arranged pores and developed an anisotropic constitutive law which is suitable for later stage sintering. We are not aware of any model in the literature which describes how the microstructure evolves around an elongate pore and predicts what factors control the anisotropic shrinkage

of a powder compact containing elongate pores. Here, we present such a model and attempts to answer these questions.

5.1. A micro-mechanical model for anisotropic sintering

We consider a two-dimensional solid consisted of hexagonal grains and periodically arranged elongate pores. Fig. 18 shows a representative unit of the solid containing only one elongate pore. No matter exchange is allowed between the representative unit and its surrounding medium. We do not consider smaller pores in the surrounding medium because such pores would have sintered first leaving the large pore behind. The hexagonal grain network is structurally anisotropic. Cocks and Searle [50] provided an analytical solution for the remote strain rates of this hexagonal grain network which deforms by grain-boundary diffusion (i.e. Coble creep). Fig. 19 shows the problem considered by Cocks and Searle [50] who derived the remote strain rates as

$$\dot{\varepsilon}_1 = -\dot{\varepsilon}_2 = 36\frac{M_{\mathrm{gb}}}{d^3}(\sigma_1 - \sigma_2) \tag{25}$$

here d is the grain size as defined in Fig. 19. Eq. (25) indicates that the creep response of the hexagonal grain structure can be treated as isotropic despite that the structure is not symmetric between its horizontal and vertical directions. Therefore, any anisotropic shrinkage in the numerical model shown in Fig. 18 must be a consequence of the elongate pore.

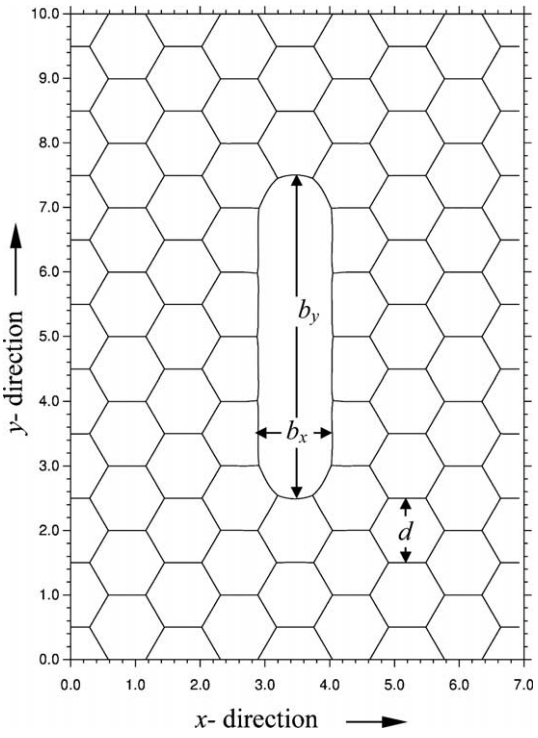

Fig. 18. A representative unit of a solid made of hexagonal grains and containing periodically arranged elongate pores. No matter exchange is allowed between the unit and its surrounding medium and periodical boundary conditions of velocity are applied at the four outer boundaries.

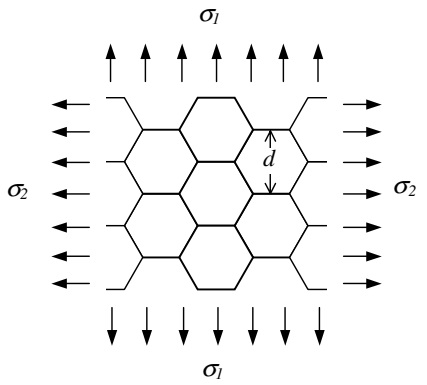

Fig. 19. A regular two-dimensional array of hexagonal grains subjected to remote stresses σ_1 and σ_2.

It is convenient to present the numerical results in a non-dimesional format. Here, we normalise all the length scales by the grain size d as shown in Fig. 18 and use a normalised time

$$\bar{t} = \frac{M_{gb}\gamma_s}{d^4}t. \tag{26}$$

Furthermore, we present the numerical results using normalised diffusion coefficient M_s/M_{gb} and grain-boundary mobility

$$\bar{M}_m = \frac{M_m d^2}{M_{gb}}. \tag{27}$$

In all the cases γ_s/γ_{gb} was set as 3, which is roughly true for many materials. The ratio of M_s/M_{gb} is varied from 0.001 to 1000, and $\bar{M}_m$ is varied from 0.1 to 1000 which covers the range of these parameters for a wide range of materials [51].

5.2. Numerical results and discussions

Fig. 20 shows the computer simulated microstructural evolution of the representative unit for $\bar{M}_m = 100$, $M_s/M_{gb} = 1$ and $\gamma_s/\gamma_{gb} = 3$. These material parameters are loosely based on alumina. In Fig. 20(a) the microstructure at four different times are superimposed on top of each other so that the overall motion of the microstructure can be seen clearly. Fig. 20(b) and (c) show the microstructure at two separate times so that one can see clearly the changes of the microstructure. It can be observed from the figures that the pore area shrinks significantly accompanied by the shrinkage of the representative unit in both x- and y-directions. The evolution of the microstructure leads to a neighbour-switching event similar to that described by Ashby and Verrall [52] for superplastic deformation. Two grains which were originally separated meet each other and a new boundary is formed between them. Fig. 20(c) shows the microstructure just before such a switching event at both ends of the elongate pore. Most of our computer simulations were terminated at this point. However, the case shown in Fig. 20 was continued after the neighbour-switching event which is shown in Fig. 37 and discussed later.

Fig. 21 shows the linear shrinkage of the representative unit in the x- and y-directions, respectively. The shrinkage anisotropy can be clearly seen from the figure. The model predicts that the representative unit shrinks more in the longer axis of the elongate pore which is in general agreement with the continuum mechanics model by Olevsky and Skorohod [49]. However, the pore spheroidisation predicted by the

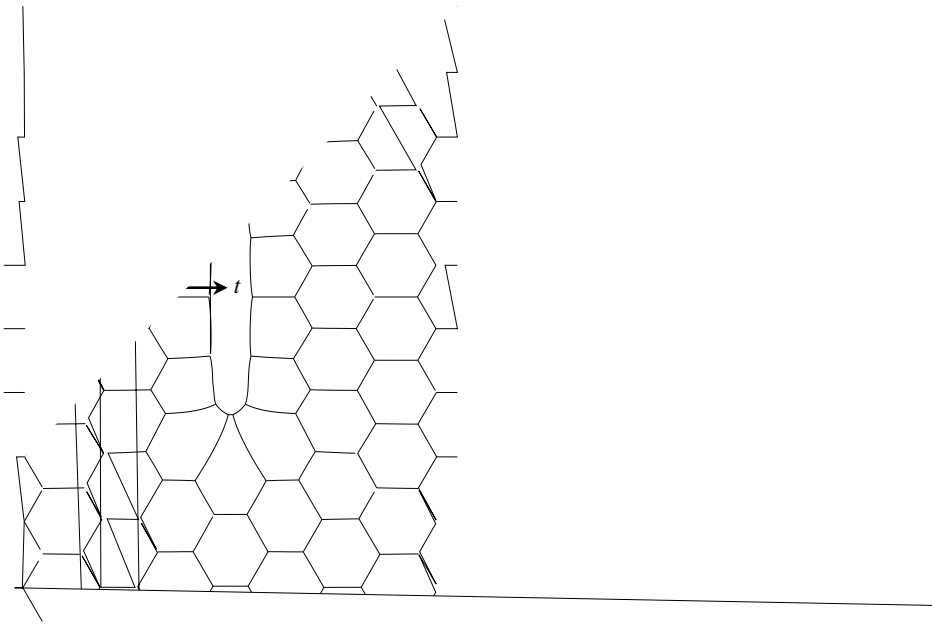
t

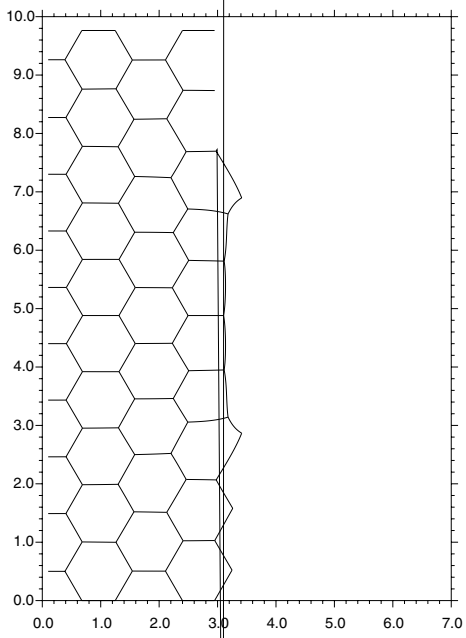
10.0
9.0
8.0
7.0
6.0
5.0
4.0
3.0
2.0
1.0
0.0
0.0
1.0
2.0
3.0
4.0
5.0
6.0
7.0

continuum mechanics model does not occur in this particular case. Fig. 22 shows the pore shrinkages in its long and short axes and the pore aspect ratio as functions of time. The micromechanical model predicts that the pore width shrinks faster than the pore length for this particular set of material parameters. Fig. 23 shows the pore area and the total free energy of the system as functions of time, which simply confirms that the pore area shrinks continuously driven by the reduction of the total free energy. Mass conservation can be taken as a measure of accuracy of the numerical model. In the simulation, the total variation of the solid area is within 0.038%.

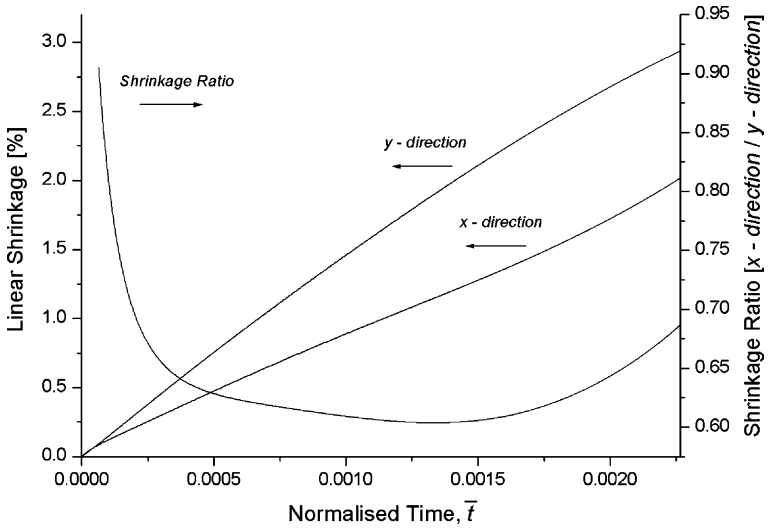

Fig. 21. The linear shrinkages of the representative unit in the x- and y-directions as functions of time. $\bar{M}_{\mathrm{m}} = 100$, $M_{\mathrm{s}}/M_{\mathrm{gb}} = 1$ and $\gamma_{\mathrm{s}}/\gamma_{\mathrm{gb}} = 3$.

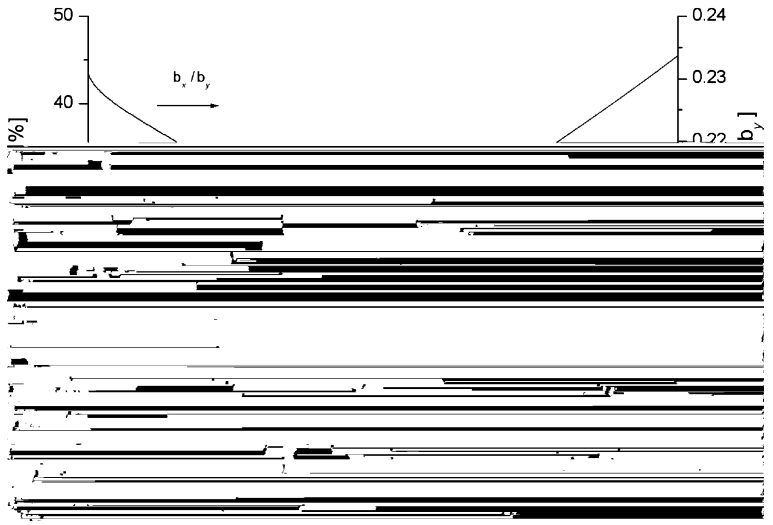

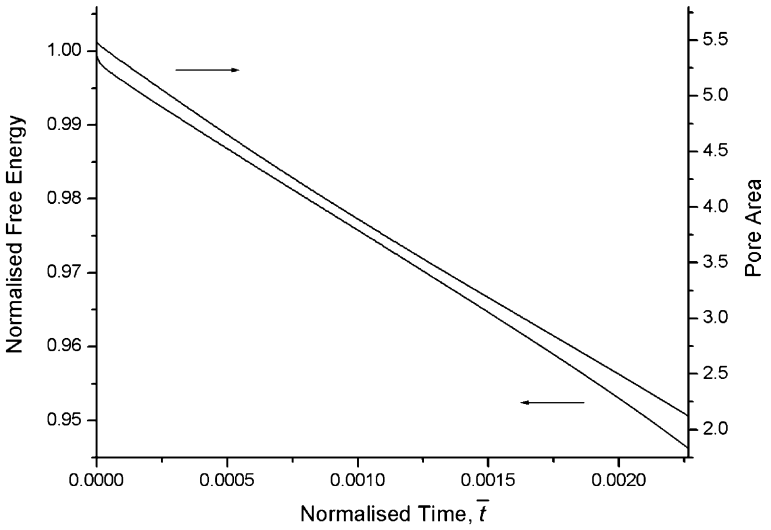

Fig. 23. Free energy and pore area as functions of time. $\bar{M}_m = 100$, $M_s/M_{gb} = 1$ and $\gamma_s/\gamma_{gb} = 3$.

5.2.1. Effect of increasing surface diffusivity

Fig. 24 presents a case in which the surface diffusion coefficient is increased by three orders of magnitude from that of the case shown in Fig. 20. All the other parameters remain to be the same. It can be seen that in the fast surface diffusion case, the pore does spheroidise as predicted by the continuum mechanics model of Olevsky and Skorohod [49]. This can also be seen from Fig. 25 which shows pore shrinkage in the two directions as functions of time. The pore width shrinks faster initially but this is quickly overtaken by the continuous shrinkage in the length of the pore. The width of the pore actually grows after the initial stage. Fig. 24 also shows that the microstructural evolution is dominated by the pore spheroidisation and the representative unit does not shrink very much by the first neighbour-switching event. Fig. 26 shows the linear shrinkages of the representative unit in the x- and y-directions, respectively, as functions of time. It can be seen from the figure that the shrinkage is less anisotropic than that for the case shown in Fig. 20 and most of the difference between the shrinkages in the two directions comes from the initial stage. The shrinkage rate of the representative unit is almost isotropic except for the initial part of the curves. An interesting observation of Figs. 25 and 26 is that the representative unit shrinks continuously in the x-direction despite that the pore width actually grows. The pore spheroidises by removing matter from the two side surfaces of the pore and depositing onto the two end surfaces. This pore spheroidisation is not necessarily accompanied by the swelling of the representative unit overall. The diffusion distance for the spheroidisation is half of the pore length and the spheroidisation becomes significant only if M_s/M_{gb} gets large enough. A series of simulations covering a wide range values of M_s/M_{gb} were carried out. It was found that the pore spheroidises if $M_s/M_{gb} > 10$ as shown by Fig. 27. The pore area and the total free energy of the system as functions of time are shown in Fig. 28.

5.2.2. Effect of increasing grain-boundary mobility

Fig. 29 presents a case in which the grain-boundary mobility has been increased by an order of magnitude from that for the case shown in Fig. 20. Because of the relatively large grain-boundary mobility, grain-growth is evident in the microstructural evolution as expected. However, the influence of grain-growth on the shrinkage anisotropy is rather unexpected. Fig. 30 shows the linear shrinkages of the representative unit in the x- and y-directions, respectively. It can be seen that the x-dimension of the representative unit remains almost unchanged while the y-dimension (in the direction of the longer axis of the pore) decreases

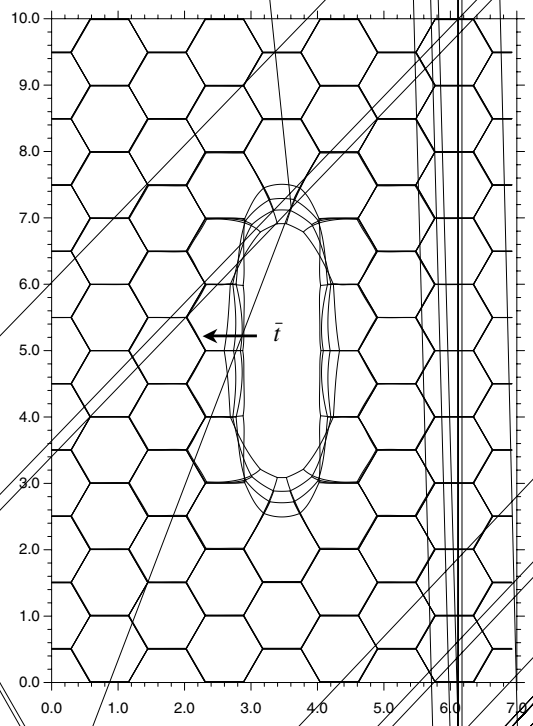
$\bar{t}$

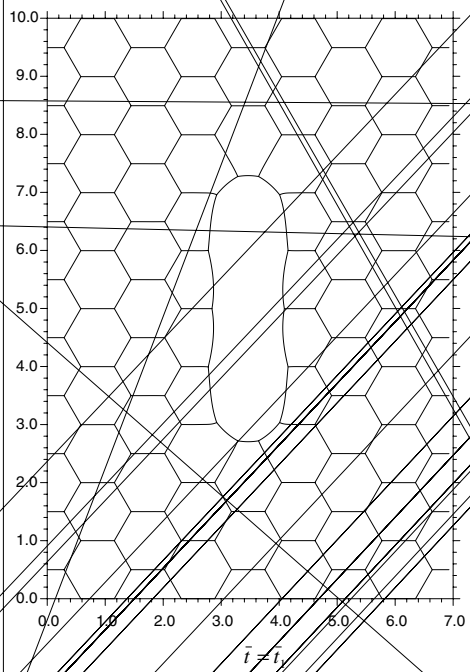
$\bar{t} = \bar{t}_1$

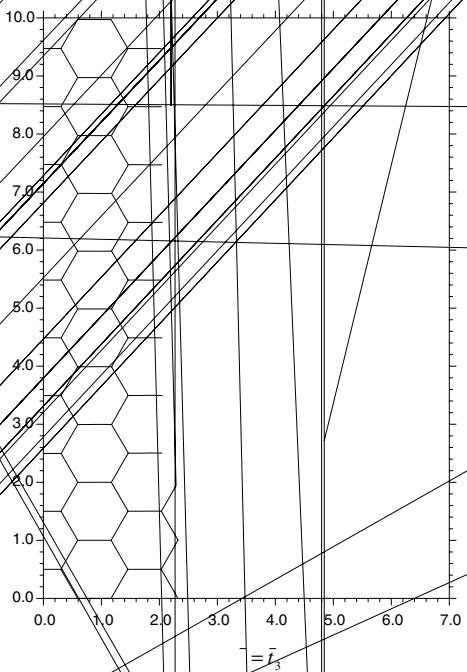
$= \bar{t}_3$

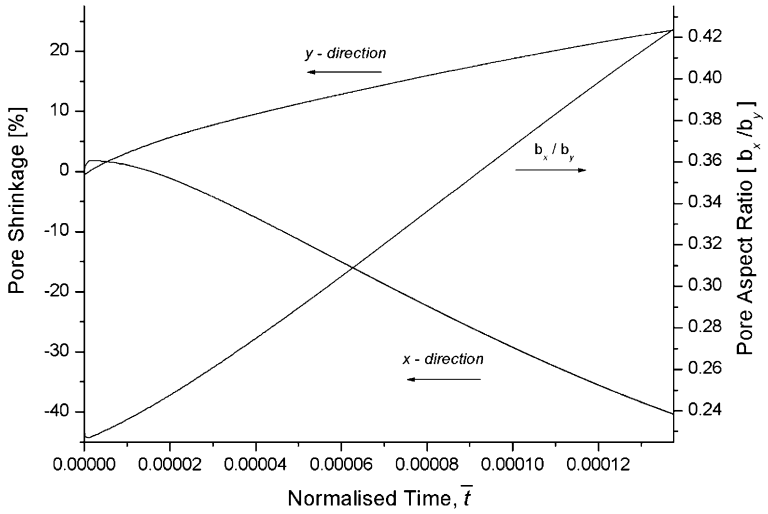

Fig. 25. Percentage change of the pore sizes in the x- and y-directions (the left vertical axis) and the pore aspect ratio as functions of time (the right vertical axis). $\bar{M}_m = 100$, $M_s/M_{gb} = 1000$ and $\gamma_s/\gamma_{gb} = 3$.

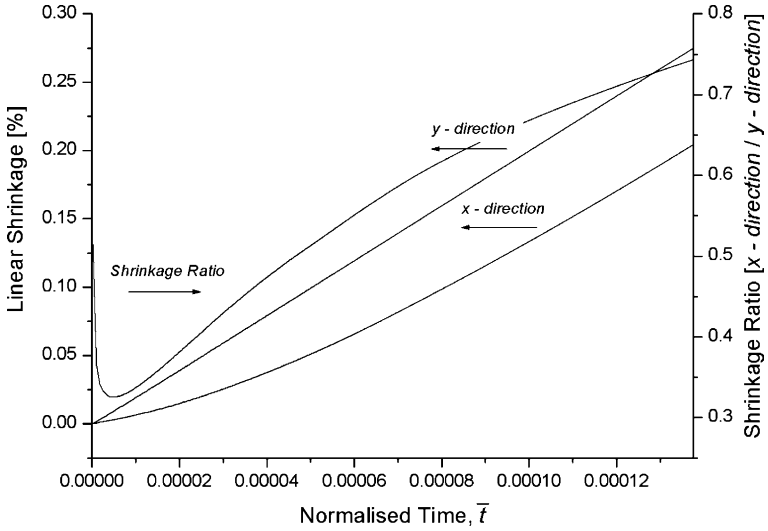

Fig. 26. The linear shrinkages of the representative unit in the x- and y-directions as functions of time. $\bar{M}_m = 100$, $M_s/M_{gb} = 1000$ and $\gamma_s/\gamma_{gb} = 3$.

continuously. It seems that the large grain-boundary mobility promotes the shrinkage anisotropy. This effect of the grain-boundary mobility on the shrinkage anisotropy is so significant that it should be able to detect the effect in a controlled experiment. We are not aware of such experimental data in the literature and it would be an interesting future work to verify this numerical finding experimentally. Fig. 31 shows the change of pore dimensions in the two directions as functions of time. It can be seen that in this case, the pore shrinks in both directions continuously and in almost equal amount. The strong anisotropic shrinkage of the representative unit is not accompanied by a strong anisotropic shrinkage of the pore. Fig. 32 shows the total free energy and the pore areas as functions of time, which is very similar to the previous cases.

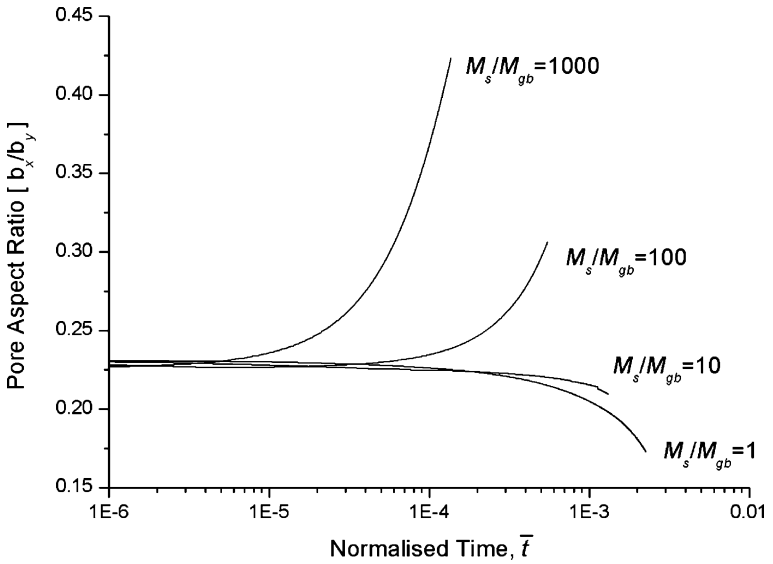

Fig. 27. The pore aspect ratio as a function of time for various values of M_s/M_{gb}. $\bar{M}_m = 100$ and $\gamma_s/\gamma_{gb} = 3$.

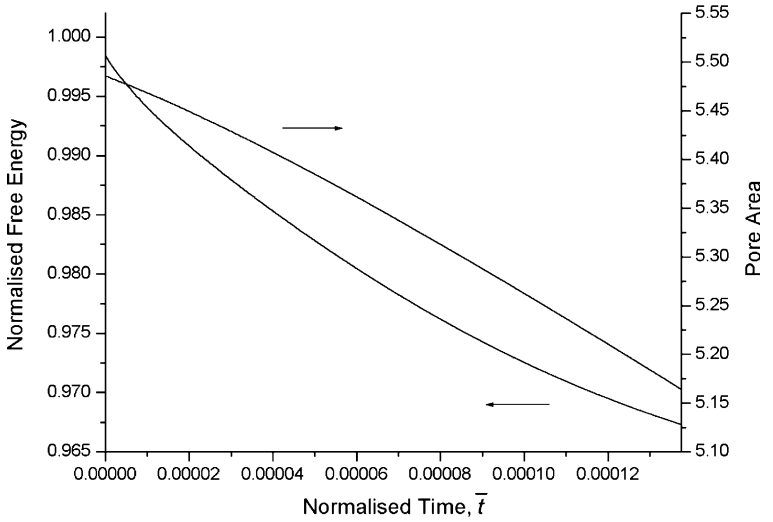

Fig. 28. Free energy and pore area as functions of time. $\bar{M}_m = 100$, $M_s/M_{gb} = 1000$ and $\gamma_s/\gamma_{gb} = 3$.

5.2.3. Effect of increasing both surface diffusivity and grain-boundary mobility

Fig. 33 presents a case in which the grain-boundary mobility has been increased by one order of magnitude, respectively, from the case shown in Fig. 24. Fig. 34 shows the linear shrinkage of the representative unit in the x- and y-directions, respectively. Fig. 35 shows the pore shrinkage and Fig. 36 shows the free energy and pore area as functions of time. Because of the fast surface diffusion, pore spheroidisation is again the main feature of the microstructural evolution. The increase of grain-boundary mobility does not make much difference to the microstructural evolution if one compares Figs. 24 and 33. However, by comparing Figs. 26 and 34, it can be seen that the fast grain-boundary migration once again makes

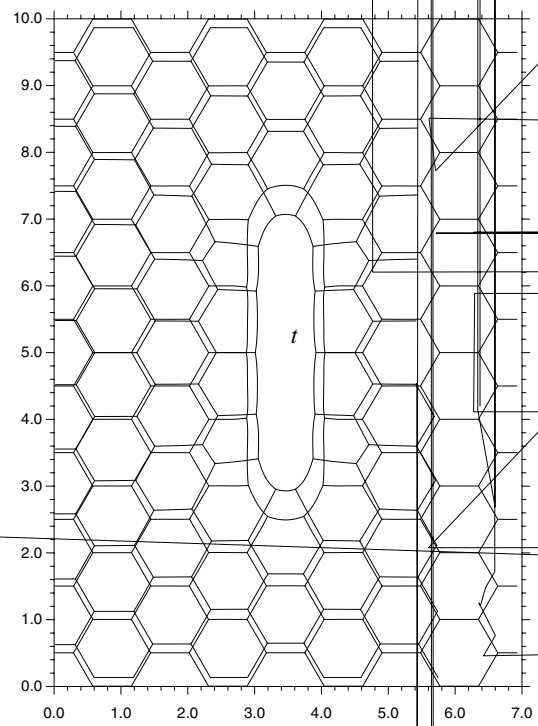

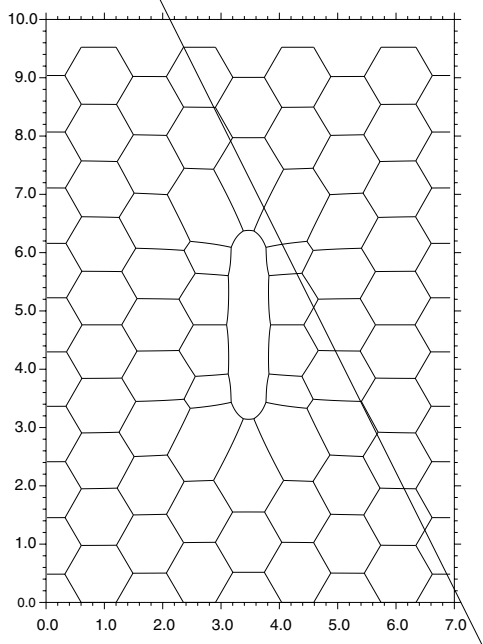

$\bar{t} = \bar{t}_2$

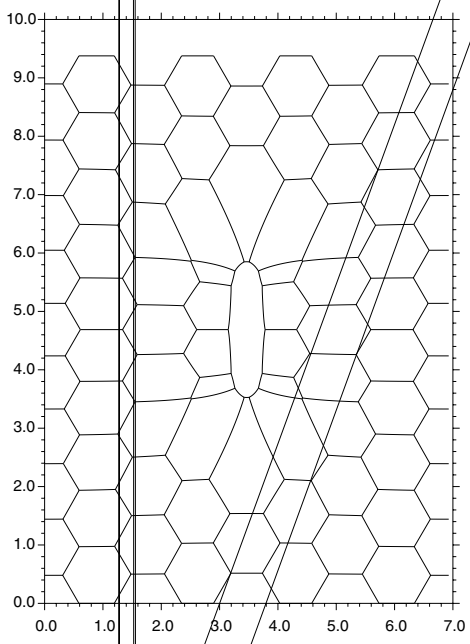

$\bar{t} = \bar{t}_3$

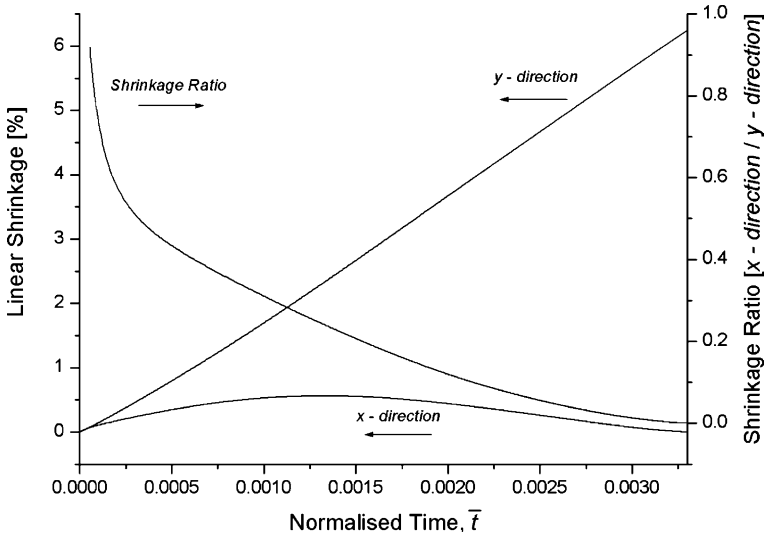

Fig. 30. The linear shrinkages of the representative unit in the x- and y-directions as functions of time. $\bar{M}_m = 1000$, $M_s/M_{gb} = 1$ and $\gamma_s/\gamma_{gb} = 3$.

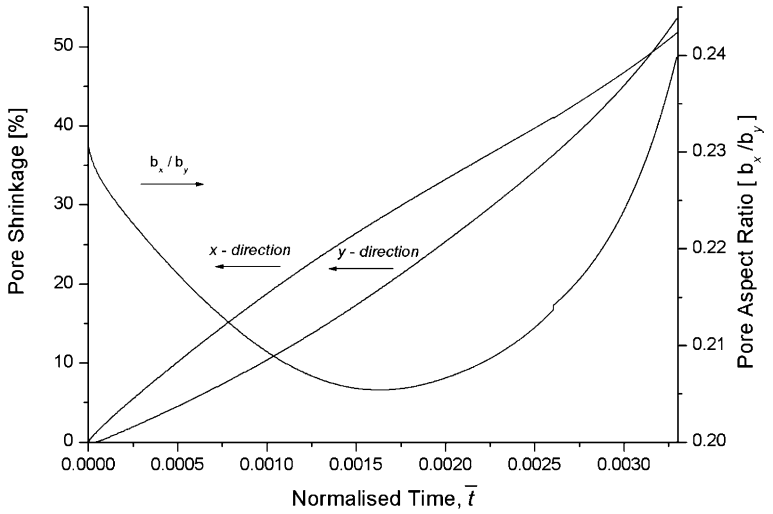

Fig. 31. Percentage change of the pore sizes in the x- and y-directions (the left vertical axis) and the pore aspect ratio as functions of time (the right vertical axis). $\bar{M}_m = 1000$, $M_s/M_{gb} = 1$ and $\gamma_s/\gamma_{gb} = 3$.

the sintering more anisotropic. It is apparent from Fig. 34 that the representative unit shrinks at a different rate in the two different directions. The shrinkage anisotropy in Fig. 26 on the other hand mainly comes from the initial stage of the process.

5.2.4. Microstructural evolution after neighbour-switching

In all the cases presented in the previous sections, the computer simulations were terminated when a section of the pore surface between two grain-boundaries becomes too short to continue the numerical analysis. The disappearance of the small section of the pore surface leads to a neighbour-switching event

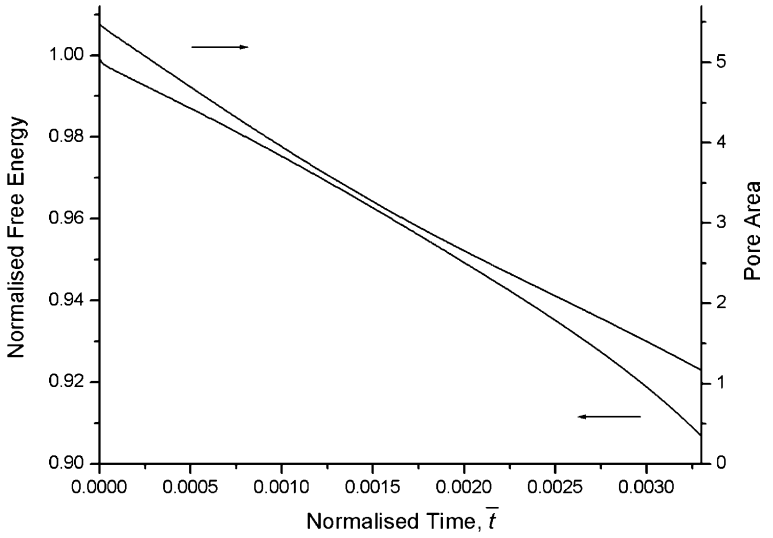

Fig. 32. Free energy and pore area as functions of time. $\bar{M}_m = 1000$, $M_s/M_{gb} = 1$ and $\gamma_s/\gamma_{gb} = 3$.

as described by Ashby and Verrall [52] for superplastic deformation. It is possible to allow such event to occur in the numerical analysis. In some of the simulations the neighbour-switching event was included and the computer simulation was continued after the topological change of the microstructure. Fig. 37 shows the continued microstructural evolution for the case shown in Fig. 20 (i.e. $\bar{M}_m = 100$, $M_s/M_{gb} = 1$ and $\gamma_s/\gamma_{gb} = 3$). The initial structure was highly symmetric about the pore and it is not possible to maintain the symmetry after a few neighbour-switching events, the microstructure becomes irregular which resembles a real microstructure. It can be observed from Fig. 37 that the neighbour-switching events make it possible for the distorted grains as shown in Fig. 20(c) to recover an equal-axis shape so that the elongate pore can shrink continuously until it disappears.

5.3. Conclusions

The numerical study presented here helps to gain some very interesting insights into the anisotropic behaviour of polycrystalline solid containing elongate pores. It is shown that the representative unit always shrinks more in the direction of the longer axis of the pore. This is in general agreement with existing experimental observations by Mitkov et al. [44] and previous models such as that by Olevsky and Skorohod [49]. More interestingly, the computer simulations show that the anisotropic shrinkage of the representative unit and the shape evolution of the elongate pore follow a complicated relationship. It was shown that the microstructural evolution and the macroscopic shrinkage are both sensitive to the relative ratios of mobilities for the surface diffusion, the grain-boundary diffusion and the grain-boundary migration. Fast surface diffusion encourages the pore to spheriodise and reduces the shrinkage anisotropy. Fast grain-boundary migration, i.e. fast grain-growth, leads to serious anisotropic shrinkage. However, the pore shrinks more or less isotropically if the grain-boundary migration is fast. The effect of fast surface diffusion is perhaps common sense and can be expected. The effect of the grain-growth on anisotropic shrinkage is, however, unexpected and requires further experimental verification. The complicated behaviour of the anisotropic shrinkage of microstructure is perhaps one of the reasons for some of the confusions in the literature on this topic. A continuum model would have to take the interplays between the various underlying microscopic processes into account in order to predict the anisotropic shrinkage successfully.

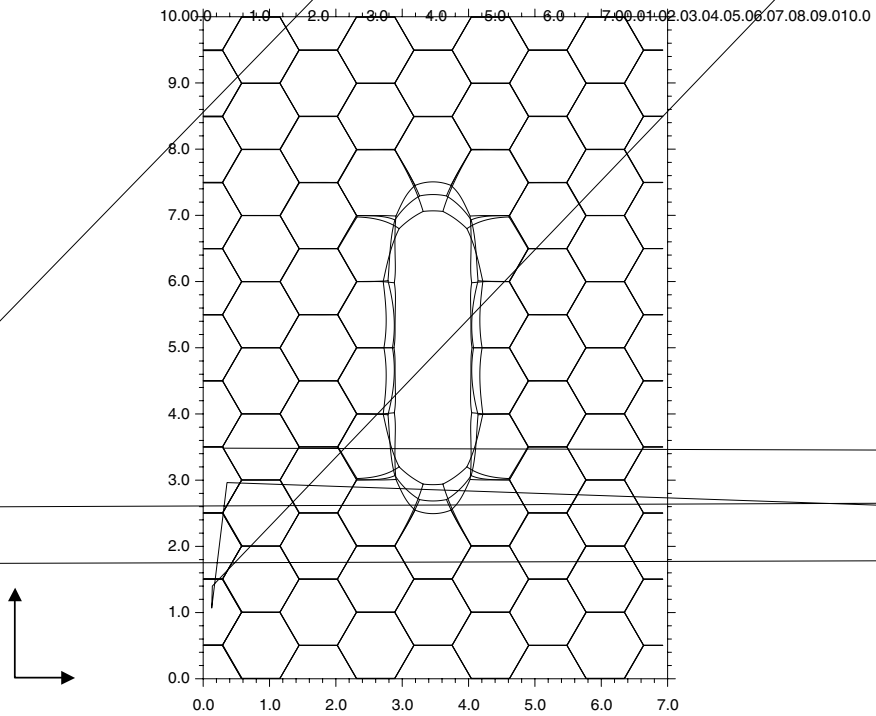

0.0 1.0 2.0 3.0 4.0 5.0 6.0 7.00.01.02.03.04.05.06.07.08.09.010.0

$\bar{t} = \bar{t}_1$ $\bar{} = \bar{t}_3$

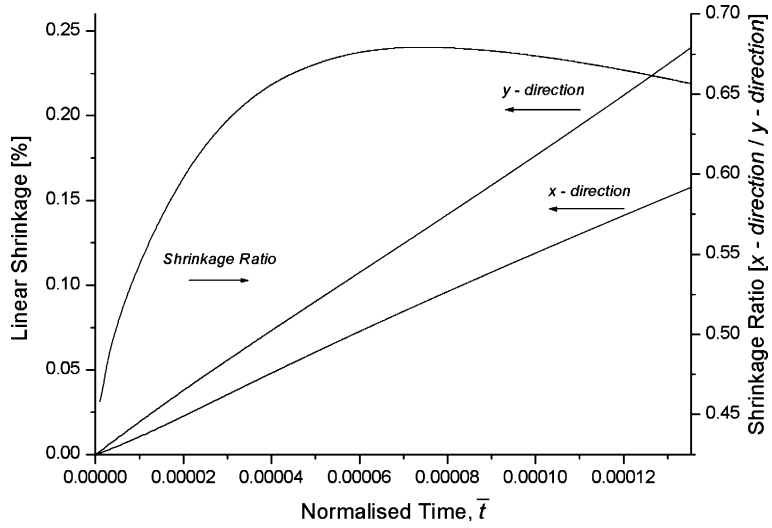

Fig. 34. The linear shrinkages of the representative unit in the x- and y-directions as functions of time. $\bar{M}_m = 1000$, $M_s/M_{gb} = 1000$ and $\gamma_s/\gamma_{gb} = 3$.

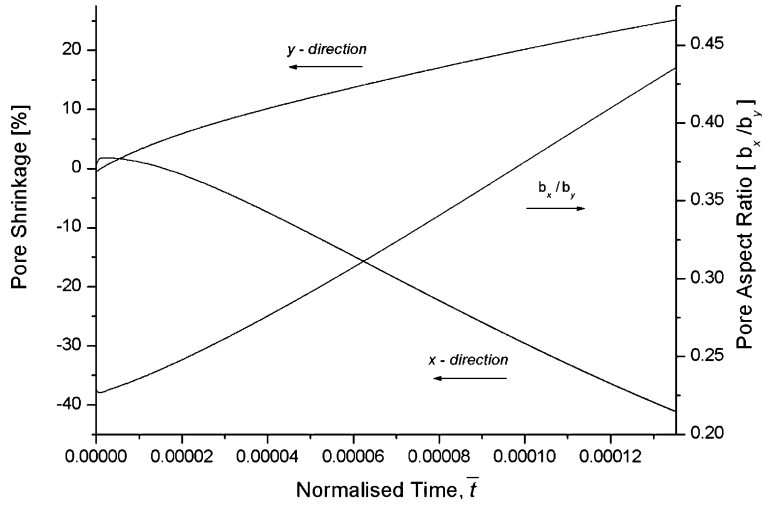

Fig. 35. Percentage change of the pore sizes in the x- and y-directions (the left vertical axis) and the pore aspect ratio as functions of time (the right vertical axis). $\bar{M}_m = 1000$, $M_s/M_{gb} = 1000$ and $\gamma_s/\gamma_{gb} = 3$.

6. Concluding remark

In conjunction with our previous paper, we have presented a complete numerical scheme which can be used to simulate microstructural evolution of materials consisted of many grains and pores assuming that grain-boundary diffusion, surface diffusion and grain-boundary migration are the operating mechanisms for matter redistribution. An application to anisotropic sintering problem has helped us to gain deep insights into the practical industrial problem. The numerical scheme is being used to study a wide range

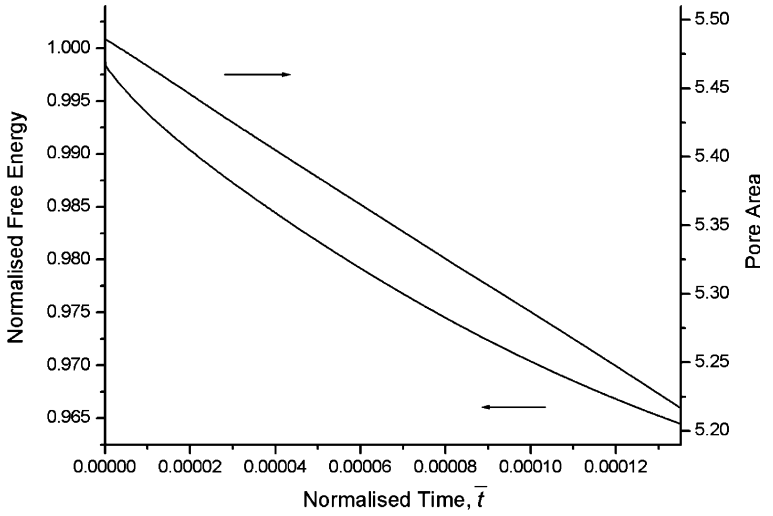

Fig. 36. Free energy and pore area as functions of time. $\bar{M}_m = 1000$, $M_s/M_{gb} = 1000$ and $\gamma_s/\gamma_{gb} = 3$.

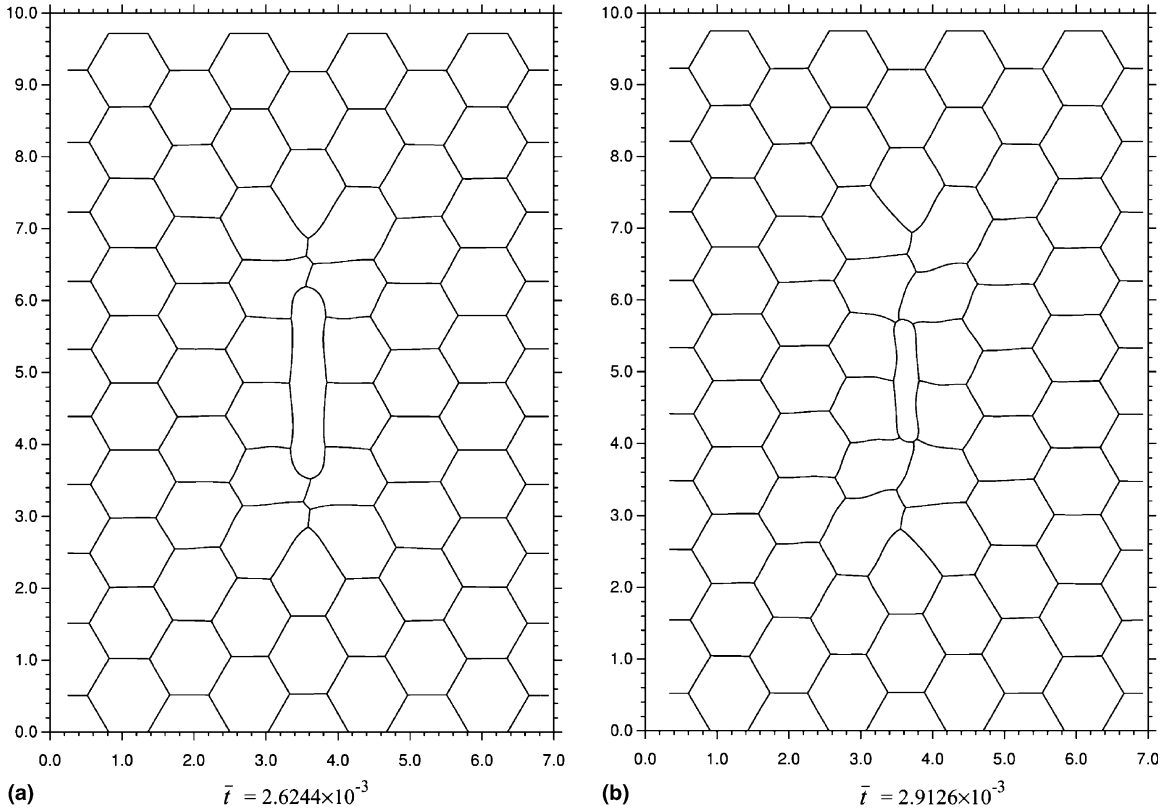

Fig. 37. Computer simulated microstructural evolution of anelongate pore in a hexagonal grain matrix after neighbour-switching event for $\bar{M}_m = 100$, $M_s/M_{gb} = 1$ and $\gamma_s/\gamma_{gb} = 3$.

of problems. For example we have used similar numerical studies to demonstrate that the critical coordination number theory for the sintering kinetics of large pores is inappropriate [53]. The variational formulations have been extended to include many more kinetic mechanisms. Elasticity, power law creep, phase transformation, vapour evaporation and condensation, interface reaction and etc have all been considered [17,23]. Robust numerical schemes based on the variational formulations have been gradually developed and perfected providing a powerful tool to study the complicated multi-physics problems involving all these processes.

Acknowledgements

This work is partially supported by an EPSRC Grant (S97996). H.N. Ch'ng also gratefully acknowledges a Ph.D. studentship from the University of Surrey.

References

[1] H.N. Ch'ng, J. Pan, Cubic spline elements for modelling microstructural evolution of materials controlled by solid-state diffusion and grain-boundary migration, J. Comput. Phys. 196 (2) (2004) 724–750.
[2] F.A. Nichols, W.W. Mullins, J. Appl. Phys. 36 (1965) 1826.
[3] P. Bross, H.E. Exner, Computer simulation of sintering processes, Acta Metall. 27 (1979) 1013.
[4] J.R. Spingarn, W.D. Nix, Diffusional creep and diffusionally accommodated grain rearrangement, Acta Metall. 26 (1977) 1389–1398.
[5] J. Svoboda, H. Riedel, Pore-boundary interactions and evolution equations for the porosity and the grain size during sintering, Acta Metall. 40 (11) (1992) 2829–2840.
[6] D. Bouvard, R.M. McMeeking, The deformation of interparticle necks by diffusion controlled creep, J. Am. Ceram. Soc. 79 (3) (1993) 666–672.
[7] W. Zhang, J.H. Schneibel, The sintering of two particles by surface and grain-boundary diffusion – a two-dimensional study, Acta Metall. 43 (1995) 4377.
[8] W. Zhang, P. Sachenko, J.H. Schneibel, I. Gladwell, Coalescence of two particles with different sizes by surface diffusion, Philos. Mag. A 82 (16) (2002) 2995–3011.
[9] S. Ling, M.P. Anderson, J. Electron. Mater. 17 (1988) 459.
[10] Y. Wang, L.-Q. Chen, Simulation of microstructural evolution, methods, Material Research, Wiley, New York, 1998.
[11] W.J. Boettinger, I.A. Warren, C. Beckermann, A. Karma, Phase-field simulation of solidification, Ann. Rev. Mater. Res. 32 (2002) 163–194.
[12] D. Wang, J. Pan, A wavelet-Galerkin scheme for the phase field model of microstructural evolution of materials, Comput. Mater. Sci. 29 (2004) 221–242.
[13] A. Needleman, J.R. Rice, Plastic creep flow effects in the diffusive cavitation of grain boundaries, Acta Metall. 28 (1980) 1315–1332.
[14] A.C.F. Cocks, A finite element description of grain-boundary controlled processes in ceramic materials, in: I.M. Allison, C. Ruiz (Eds.), Applied Solid Mechanics – 3, Elsevier, North-Holland, Amersterdam, 1989.
[15] J. Pan, A.C.F. Cocks, Computer simulation of superplastic deformation, Comput. Mater. Sci. 1 (1993) 95–109.
[16] J. Pan, A.C.F. Cocks, S. Kucherenko, Finite element formulation of coupled grain-boundary and surface diffusion with grain-boundary migration, Proc. R. Soc. Lond. A 453 (1997) 2161–2184.
[17] A.C.F. Cocks, S.P.A. Gill, J. Pan, Modelling microstructure evolution in engineering materials, Adv. Appl. Mech. 36 (1999) 81–162.
[18] B. Sun, Z. Suo, W. Yang, A finite element method for simulating interface motion – I. Migration of phase and grain boundaries, Acta Metall. 45 (1996) 1907–1915.
[19] B. Sun, Z. Suo, A finite element method for simulating interface motion – II. Large shape change due to surface diffusion, Acta Metall. 45 (1997) 4953–4962.
[20] E. Bänsch, P. Morin, R.H. Nochetto, Finite element methods for surface diffusion, in: Proceedings of Free Boundary Problems: Theory and Applications, Trento, 2002 (to appear).
[21] J.S. Chen, V. Kotta, H. Lu, D. Wang, D. Moldovan, D. Wolf, A variational formulation and a double-grid method for meso-scale modeling of stressed grain growth in polycrystalline materials, Comput. Meth. Appl. Mech. Eng. 193 (2004) 1277–1303.

[22] Z. Suo, Z. Wang, Diffusive void bifurcation in stressed solid, J. Appl. Phys. 76 (1994) 3410–3421.
[23] A.C.F. Cocks, S.P.A. Gill, A variational approach to two dimensional grain-growth I. Theory, Acta Metall. 44 (1996) 4765–4775.
[24] W.W. Mullins, The effect of thermal grooving on grain-boundary migration, Acta Metall. 6 (1958) 414–427.
[25] W.W. Mullins, Theory of thermal grooving, J. Appl. Phys. 28 (1957) 333–339.
[26] Z. Suo, Motions of microscopic surfaces in materials, Adv. Appl. Mech. 33 (1997) 193–294.
[27] J. Pan, A.C.F. Cocks, A numerical technique for the analysis of coupled surface and grain-boundary diffusion, Acta Mater. 43 (1995) 1395–1406.
[28] J. Pan, Modelling sintering at different length scales – a critical review, Int. Mater. Rev. 48 (2003) 69–85.
[29] R.M. German, Sintering Theory and Practice, Wiley, New York, 1996.
[30] L.E. Sanchez, Electric, mechanical and thermal characterization of a co-fired multilayer substrate processes from sol-gel silica, in: M.F. Yan, K. Niwa, H.M. O'BryanJr., W.S. Young (Eds.), Advances in Ceramics, Ceramic Substrates and Packages for Electronic Applications, vol. 26, Am. Ceram. Soc., Westerville, OH, 1989, pp. 387–397.
[31] M. Mitomo, S. Saito, T. Matsuda, T. Yonezawa, Sintering anisotropy in slip-cast SiC-whisker/Si_3N_4-powder compacts, J. Mater. Sci. 28 (1993) 5548–5553.
[32] J. Huber, W. Krahn, J. Ernst, A. Bocker, H.J. Bunge, Texture formation in Al_2O_3 substrates, Mater. Sci. Forum 157–169 (1994) 1411–1416.
[33] T. Zhang, S. Blackburn, J. Bridgwater, Debinding and sintering defects from particle orientation ceramic injection moulding, J. Mater. Sci. 31 (11) (1996) 5891–5896.
[34] K. Uematsu, S. Ohsaka, N. Shinohara, M. Okumiya, Grain-oriented microstructure of alumina ceramics made through the injection moulding process, J. Am. Ceram. Soc. 80 (5) (1997) 1313–1315.
[35] R. Greenwood, E. Roncari, C. Galassi, Preparation of concentrated aqueous suspensions for tape casting, J. Eur. Ceram. Soc. 17 (12) (1997) 1393–1401.
[36] P.M. Raj, W.R. Cannon, Anisotropic shrinkage in tape-cast alumina: role of processing parameters and particle shape, J. Am. Ceram. Soc. 82 (1999) 2619–2625.
[37] P.M. Raj, A. Odulena, W.R. Cannon, Anisotropic shrinkage during sintering of particle-oriented systems – numerical simulation and experimental studies, Acta Mater. 50 (2002) 2559–2570.
[38] A. Shui, M. Saito, N. Uchida, K. Uematsu, Development of anisotropic microstructure in uniaxially pressed alumina compacts, J. Eur. Ceram. Soc. 22 (2002) 1217–1223.
[39] A. Shui, N. Uchida, K. Uematsu, Origin of shrinkage anisotropy during sintering for uniaxially pressed alumina compacts, Powder Tech. (2002).
[40] A. Shui, Z. Kato, S. Tanaka, N. Uchida, K. Uematsu, Sintering deformation caused by particle orientation in uniaxially and isostatically pressed alumina compacts, J. Eur. Ceram. Soc. 22 (2002) 311–316.
[41] O.V. Roman, H.H. Hausner, Investigation in the linear shrinkage of metal powder compacts during sintering, J. Jpn. Soc. Powder Metall. 9 (1962) 228–236.
[42] H.H. Hausner, The linear shrinkage behaviour of metal powder compacts during sintering, Prog. Powder Metall. 19 (1963) 67–85.
[43] H.E. Exner, New models for theoretical description of sintering processes, Monograph, Stuttgart, 1976.
[44] M. Mitkov, H.E. Exner, G. Petzow, Orientation of pore structure in loose and presses carbonyl iron and its influence on shrinkage anisotropy, Sintering – New Developments (1979) 90–98.
[45] M.N. Rahaman, L.C. De Jonghe, Sintering of spherical glass powder under a uniaxial stress, J. Am. Ceram. Soc. 73 (3) (1990) 707.
[46] G. Arghir, G.C. Kuczynski, Short note: anisotropic shrinkage of copper compacts, Powder Metall. Int. 10 (2) (1978) 73.
[47] H.I. Moon, W.J. Huppmann, Short note: change of shrinkage anisotropy during sintering, Powder Metall. Int. 6 (3) (1974) 143.
[48] A. Jagota, P.R. Dawson, J.T. Jenkins, An anisotropic continuum model for the compaction of powder packings, Mech. Mater. 7 (1988) 255.
[49] E.A. Olevsky, V. Skorohod, Deformation aspects of anisotropic-porous bodies sintering, J. Phys. IV C7 3 (1993) 739.
[50] A.C.F. Cocks, A.A. Searle, Cavity growth in ceramic materials under multiaxial stress states, Acta Metall. 38 (1989) 2493.
[51] M.F. Ashby, Hip 6.0 background reading, Engineering Department, Cambridge University, 1990.
[52] M.F. Ashby, A.A. Verrall, Diffusion accommodated flow and superplasticity, Acta Metall. 21 (1973) 149–163.
[53] J. Pan, H.N. Ch'ng, A.C.F. Cocks, Sintering kinetics of large pores, Mech. Mater (accepted).